Optical and Electrical Properties of Thin Film $BaSnO_3$

Author
Dave Mack
OSU Department of Physics
12/07/10

Senior Thesis 2010
Advisor
Prof. Janet Tate

Abstract

Thin films of the perovskite barium tin oxide ($BaSnO_3$) were prepared and characterized by their structural optical, electrical, and photoluminescent characteristics. Film deposition methods included both RF sputtering and pulsed laser deposition techniques. High quality, oriented films having optical bandgaps ranging between 3.7 eV & 4.4 eV were produced on various substrates. The undoped films were both highly insulating and transparent, making them potential candidates in gas-sensor applications and as insulating layers in transparent transistors. They did not show evidence of photoluminescence that had been reported in the bulk. Films doped with potassium, indium and lanthanum remained highly transparent but failed to exhibit any semiconducting characteristics.

TABLE OF CONTENTS

INTRODUCTION/BACKGROUND

This research studies the optical and electric properties of barium tin oxide $BaSnO_3$ thin films grown using both RF magnetron sputtering and pulsed-laser deposition techniques.

The thin-film form of $BaSnO_3$ (BTO) was initially selected for research with the purpose of investigating its viability as a *p*-type transparent semiconductor. While several varieties of *n*-type transparent semiconductors have been developed, a *p*-type material of comparable electrical conductivity has remained elusive. In fact, *p*-type transparent semiconductors trail their *n*-type counterparts in conductivity by two to three orders of magnitude. Development of a comparable *p*-type variety of transparent semiconductor will undoubtedly advance the science of a myriad of electronic devices including flat-panel displays, solar cells and optical emitters. As the research progressed, the thin-film form of BTO was also studied for its potential as an *n*-type transparent semiconductor, its photoluminescent properties and its characteristics as an insulator.

BTO has proven to be a rather versatile compound, though most of the work that has been done regarding its properties has been on the pressed powder form of the material though some thin film work has been reported [1-3]. In pure form, below 1000°C, BTO behaves as an intrinsic *n*-type semiconductor finding application as a high-dielectric thermally stable capacitor [4,5]. Capacitors possessing these traits are becoming increasingly important as the physical size of electronic devices continues to shrink. Pressed powder studies concerning the semiconducting behavior of BTO have shown that through controlled doping, the compound transitions into an n-type semiconductor when doped with lanthanum and a p-type semiconductor when doped with cobalt [6,7]. In both undoped and doped form, BTO is attractive as a sensing device for an assortment of gases including Cl_2, CO, NO_x, CH_4, and liquefied petroleum gas (LPG), to name a few [8,9]. It is desirable to create thin films that exhibit these same characteristics. The compound has also been found to exhibit strong near-infrared (NIR) photoluminescence [10] – a phenomenon quite rare in a material that can also become an electrical conductor. BTO powders are white; white powders typically reveal themselves as transparent thin films. True to form, results of this study confirm, BTO films are optically transparent at visible wavelengths.

$BaSnO_3$ (BTO) bears the structural classification "perovskite" being further categorized as an alkaline-earth stannate. Other earth stannates include $CaSnO_3$ and $SrSnO_3$. BTO is further classified as an "ideal cubic perovskite" (space group $Pm\bar{3}m$), whereas many perovskite compounds suffer octahedral tilting distortion that skews the cubic structure. The general form of the perovskite structure is ABO_3 where the A cation has a "two-plus" charge and the B cation has a "four-plus" charge. The A^{2+} ion is at the center of the cube (green) and is surrounded by the B^{4+} ions (blue) located at what would be the four corners of the cube. Each of the A^{2+} ions is surrounded by 12 oxygen atoms (red) and each B^{4+} ion is surrounded by 6 oxygen atoms. The A-O and B-O bond strengths (Pauling) form ratios of $2/12$ and $4/6$ respectively [12]. As such, in the specific case of barium tin oxide, we have: $Ba^{2+}Sn^{4+}[O^{2-}]_3$. The barium ion is located at the center of the cube surrounded by the tin ions, which are in turn surrounded by the oxygen atoms, which form SnO_6 octahedra.

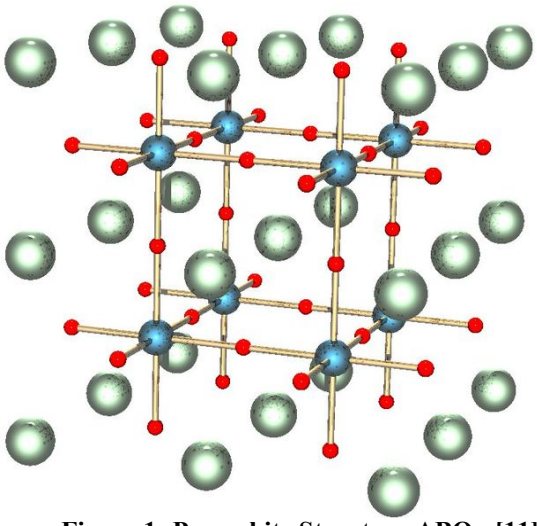

Figure 1: Perovskite Structure ABO_3. [11]

Because the structure is cubic, the Sn-O-Sn bond is 180°, and the O-Sn-O bond angle is 90°. Furthermore, the Sn-O intra-atomic length is 2.055 Å while the Ba-O bond length is 2.905 Å [13]. The theoretical density of $BaSnO_3$ is 7.24 g/cm^3.

The X-ray diffraction (XRD) spectra of $BaSnO_3$ prepared through the solid state method shown in Figure 2 corresponds to the to the XRD pattern given by the Joint Committee on Powder Diffraction Standards (JCPDS) file 74-1300. This powder diffraction file also reports the lattice parameter of BTO as 4.1085(15) Å.

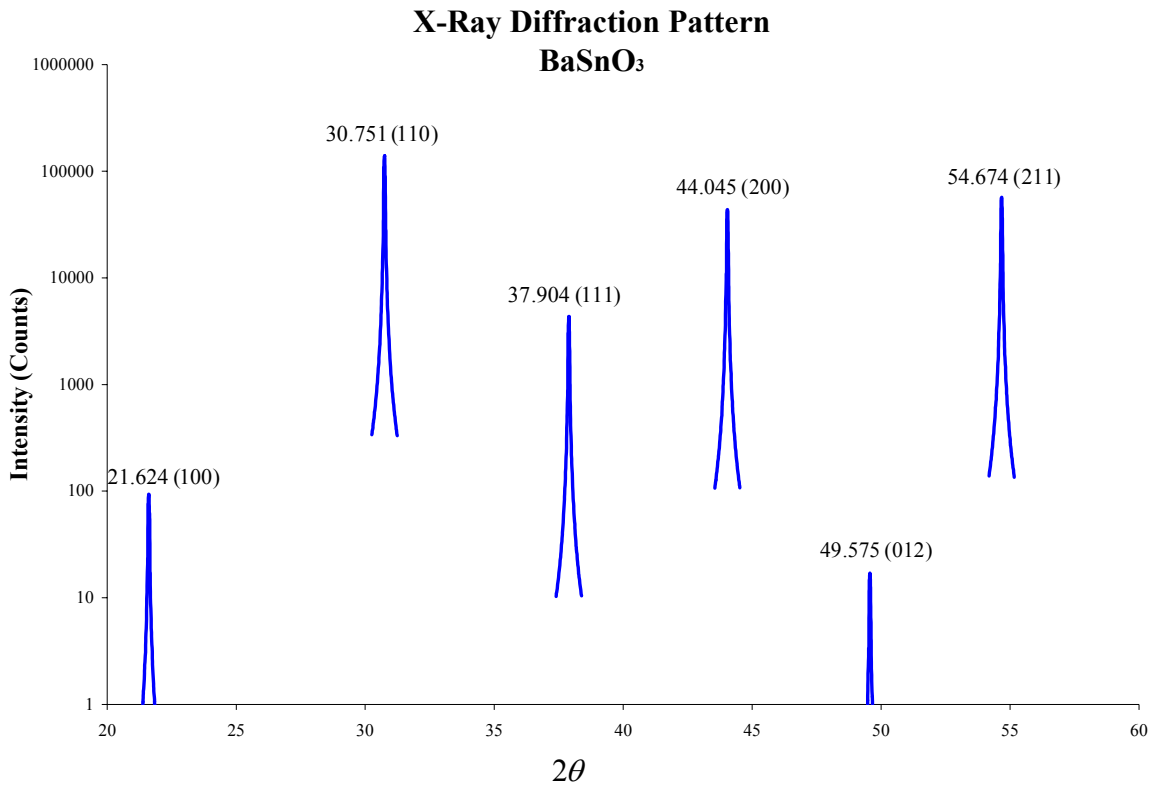

Figure 2: BTO XRD Pattern

Band Structure

The following discussion follows Mizoguchi et al. [13]. The band structure and density of states for BTO is shown below and was created using the Linear Muffin-Tin Orbital (LMTO) code. In order to understand the meaning of the horizontal labels, the Brillouin zone of the primitive cubic lattice is shown in Figure 3 to the right.

Figure 4 illustrates the use of "fatbands," the widths of which are indicators of the relative contributions of the various atomic orbitals to a given band. The bands are color coded for easy reference with respect to a given atomic orbital. In the left hand diagram, red, blue and green correspond to the Sn-5s, Sn-5p, and Ba-6s atomic orbitals respectively. In the center

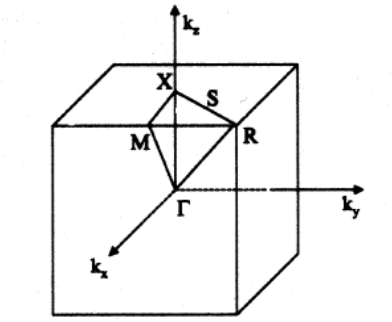

Figure 3: The Brillouin zone of cubic $BaSnO_3$ [13]

diagram the red and blue colors correspond to the O-2s and O-2p atomic orbitals, and in the density of states (DOS) diagram on the right, the green, red, and blue colors correspond to the Ba-6s, Sn-5s, and Sn-5p respectively. The total DOS is shown in black.

It appears from Figure 4 that the Sn-5s orbital which is largely responsible for the conduction band (CB) minimum while the valence band (VB) maximum seems to be largely composed of O-2p orbitals.

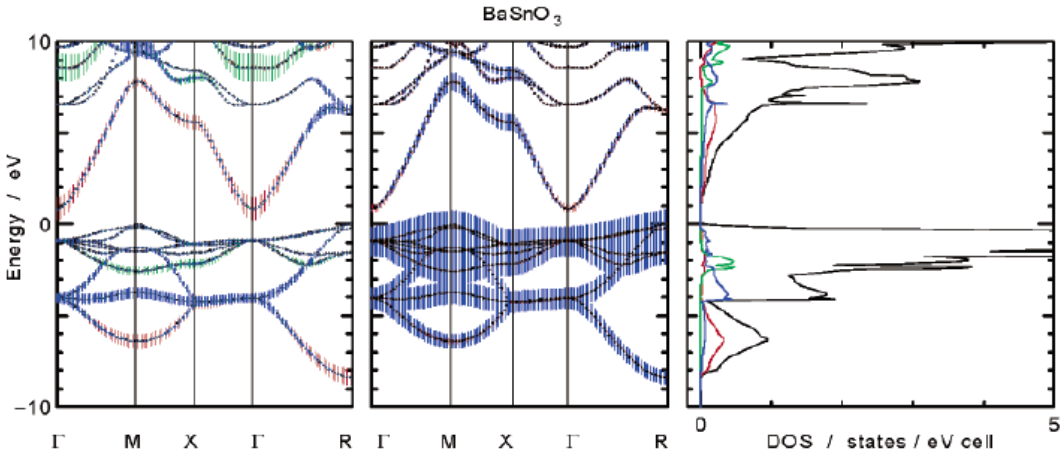

Figure 4: Band Structure of BTO [13]

The first notable feature is that BTO is evidently an indirect bandgap material. The bottom of the CB is located at the Γ point while the top of the valence band (VB) is located at points M and R. The bandgap, the minimum difference between the top of the valence band and the bottom of the conduction band, appears to be just under 1eV. By contrast, the literature quotes experimental bandgap values between 3.1eV and 3.4eV [6,10]. It is known that LMTO as well as density functional theory (DFT) systematically understate bandgap values, so this result is expected.

A second interesting feature is the large curvature at the Γ point at the bottom of the conduction band. A large curvature is consistent with a small effective mass since $1/m^* \alpha \partial^2 E/\partial k^2$. A small effective mass translates to high carrier mobility when scattering effects are negligible. A subtler feature is the difference in energy between the two lowest conduction bands at the Γ point. This large gap (~ 6eV) is characteristic of a good TCO as it limits the optical absorbance by conduction band carriers in the spectral range between the visible and IR wavelengths.

Semiconductor Studies

As previously stated, BTO is an intrinsic n-type semiconductor with an experimentally measured indirect bandgap energy between 3.1eV and 3.4eV. Theoretically, doping BTO with either acceptor or donor ions should allow for the onset of electrical conductivity. For example, substituting a potassium ion, K^{+}, on the Ba^{2+} site should result in a *p*-type semiconductor, or substituting a lanthanum ion, La^{3+}, on the Ba^{2+} site should result in an *n*-type semiconductor. It is also theoretically possible to substitute acceptors or donors on the Sn^{4+} site as well. Whether or not an ion will substitute onto a particular site is largely determined by two factors: 1) The comparative atomic radii of the original atom and the dopant ion, and 2) The comparative valence state of the original atom and the possible states of the dopant ion.

Peer-reviewed articles revealed two studies of doping BTO in an attempt to "create" a semiconducting device. Both studies were interested in the electrical conductivity but neither indicated an interest in optical transparency.

The first study, created pressed powder samples of $BaSnO_3$ doped with three different concentrations (0.1%, 1.0% & 5.0%) of lanthanum [6]. It was found that La^{3+} substituted onto the Ba^{2+} site which caused the material to function as an n-type semiconductor. The ionic radii of La^{3+} and Ba^{2+}, 1.2 Å and 1.5 Å respectively [14], seems to reasonably satisfy the atomic radii criteria stated above. The crystal structure remained cubic due to the low dopant concentrations, though the average lattice parameter decreased from 4.123 Å to 4.114 Å attributable to the smaller ionic radius of La^{3+}. Electrical conduction (Figure 5.) was attributed to oxygen vacancies created during the synthesis process and subsequent cooling. It was theorized that the sharp increase in conductivity between the undoped sample and that doped with 5% lanthanum was due to Sn^{4+} ions created during the synthesis process changing states from Sn^{2+} and Sn^{3+} through electron capture.

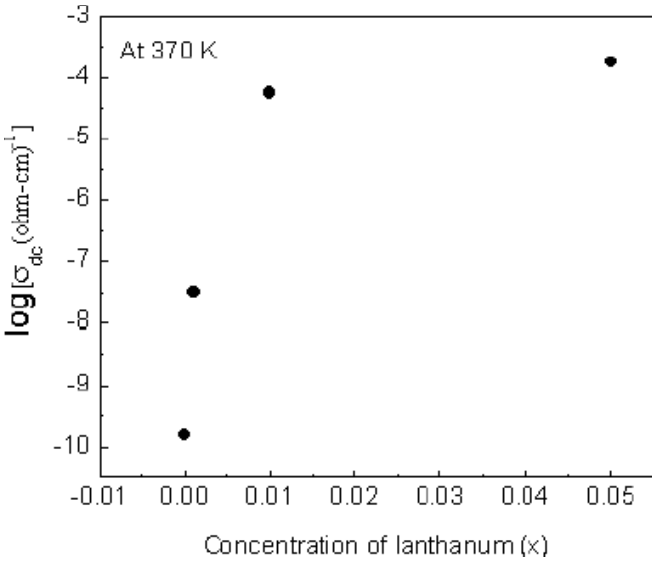

Figure 5: Electrical conduction of Lanthanum doped $BaSnO_3$ [6]

The second study followed essentially the same methodology as the previous one. Pressed powder samples of three cobalt dopant concentrations (1%, 5%, & 10%) were synthesized [7]. Since the ionic radii of Co^{3+} (0.72 Å) and Sn^{4+} (0.70 Å) are nearly the same, cobalt ion substitution onto the Sn^{4+} site would seem likely. Substitution of this configuration would create an overall deficit of electrons, the result being the creation of a *p*-type semiconductor. To determine this, the scientists conducting this study employed the use of the *Seebeck Effect* from which they determined that the majority charge carriers were positive, i.e., "holes." Figure 6 shows the results for 5% and 10% cobalt doping concentrations.

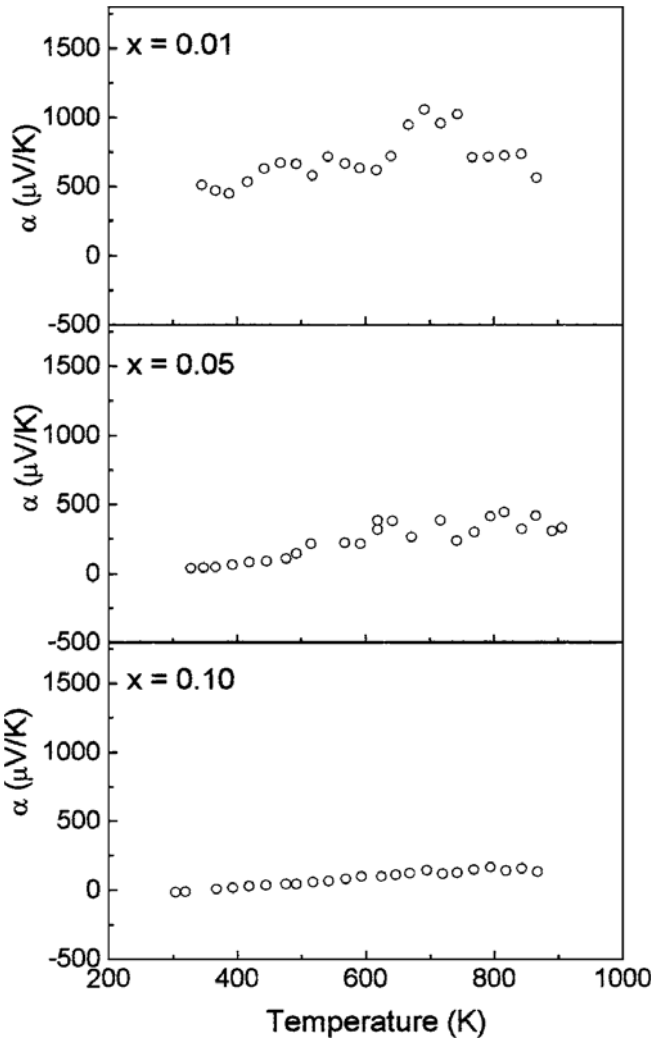

Figure 6: Correlation of Seebeck coefficient with temperature. [7]

Photoluminescence Studies

A study by Mizoguchi et al. [10] of Sr-doped BTO powder $Ba_{1-x}Sr_xSnO_3$ revealed near-infrared (NIR) photoluminescence (PL) when the material was excited at the wavelength corresponding to its bandgap energy 3.26 eV. The excitation wavelength can be calculated as 1240 eV nm/3.26 eV = 380 nm. NIR PL was rather unexpected, as luminescence in tin oxides has typically been observed in the 300 nm – 700 nm range. In this case, photoluminescence was observed in the near-infrared region (905 nm) at room temperature (Figure 7). The paper speculates that this is due to the presence of Sn^{2+} ions, which create a defect state positioned approximately 1.4 eV above the valence band. The creation of the Sn^{2+} ions is in response to the formation of oxygen vacancies due to high temperature annealing. When holes in the valence band and electrons occupying an interstitial state below the conduction band recombine, photons in the NIR are emitted. This Figure 7 also shows that the NIR photoluminescence decreases with decreasing temperature while the visible PL increases with decreasing temperature.

It was also observed that photoluminescence is strongest with undoped BTO and decreases as strontium increases ($Ba_{1-x}Sr_xSnO_3$) and barium decreases. Figure 8 shows the shift in PL wavelength with respect to Sr doping concentrations. The authors assert that thin films of BTO may also exhibit the luminescent qualities exhibited by the powder form and suggest this as course of study.

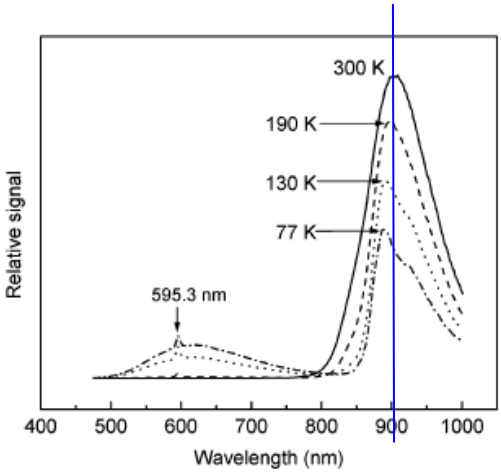

Figure 7: Photoluminescence of $BaSnO_3$ with respect to temperature. [10]

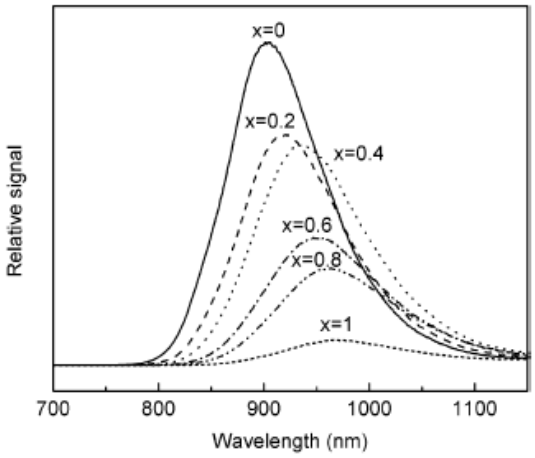

Figure 8: Shift of photoluminescence in $Ba_{1-x}Sr_xSnO_3$ with Sr dopant levels. [10]

In a study on another perovskite, strontium tin oxide ($SrSnO_3$) photoluminescence was evident at 425 nm and 77 K [15]. In that case the photoluminescence decreased with increasing temperature. The authors' explanation for the PL mechanism was band-to-band absorption (Figure 9). That is, electrons promoted to the conduction band form small polarons, which in turn interact with holes resulting in self-trapped excitons. It is the recombination of the excitons that generates the photoluminescence.

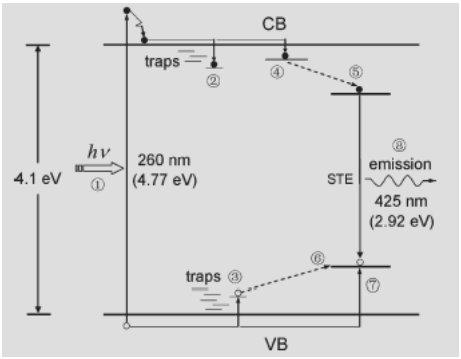

Figure 9: Proposed mechanism for photoluminescence in $SrSnO_3$. [15]

Finally, in a third study, thin films of amorphous $BaTiO_3$ (also a perovskite) exhibited room temperature photoluminescence in the visible spectrum [16]. Like the NIR PL in BTO, there was a strong correlation between heat treatment and the PL. There was an equally strong correlation between PL and the level of structure in the films. Amorphous films exhibited PL, but as the films became more ordered, i.e., the defect concentration decreased, the PL dropped off. Unlike the previous study, these scientists concluded that the mechanism for the photoluminescence could not be band-to-band transitions because the excitation energy (2.52 eV) was less than the bandgap energy (3.7 eV).

METHODS

TARGET FABRICATION

All of the targets used for this research were fabricated by the OSU Chemistry Department and fall into two broad categories: doped and undoped. Targets doped with potassium and indium were used in the sputter chamber while the undoped targets and lanthanum-doped targets were used in the PLD chamber.

Sputter Targets

The 2-inch diameter targets used in the sputter chamber were fabricated by pressing a powder of BTO at 5 tons and then them at annealing at 1375 ºC for 10 h in air. The powders were prepared by heating a mixture of the reagents $BaCO_3$ (Cerac, 99.9%) and SnO_2 (Cerac, 99.99%) at 1175 ºC for 6 h. No details on the doping reagents are available but targets were said to contain a 10% doping level for both the potassium and indium doped targets. The sputter targets appeared primarily white with a slight yellow hue. The density of the $BaSnO_3$:K target was 65% of theoretical density, while the density of the $BaSnO_3$:In target was not measured.

PLD Targets

The 1-inch diameter targets used in the PLD chamber were fabricated in the similar fashion to those created for sputtering. The starting materials for the La-doped targets, were $BaCO_3$ (Cerac, 99.9%), SnO_2 (Cerac, 99.9%), and La_2O_3 (Cerac 99.99%). The reagent powders were pressed and heated to 1100° C. The targets were then reground, repressed and annealed a second time. Three targets were fabricated with doping levels of 1% (ρ = 60.5%), 5% (ρ = 50%), and 10% (ρ = 53%). No detailed information is available regarding the fabrication of the undoped target. The PLD targets appeared light blue/grey with blue flecks.

DEPOSITION

Sputtered Films

Sputtering is one of a number of common thin film deposition processes. Although sputtering processes have evolved over time in type and sophistication, sputtering, in all of its forms is essentially a momentum transfer process.

A target, formed into the desired compound is affixed to a metal backing plate and then mounted inside an evaporation chamber. A substrate, onto which the target material is to be deposited, is mounted inside the chamber facing the target. The target then functions as the cathode of the system whilst the substrate mount serves as the anode. The chamber is subsequently evacuated and an inert gas (typically argon) is introduced into the chamber. A potential difference is set up between the target and substrate and thus across the gas. The increase in pressure due to the introduction of the gas, in concert with a sufficiently large voltage creates a glow discharge which, in turn, ionizes the gas. Positive ions, attracted to the negative potential of the target, accelerate toward and strike the target ejecting atoms from it. The liberated atoms subsequently coat the substrate creating a thin film of the desired material. Secondary electrons emitted from the cathode sustain the plasma.

A variety of materials can be deposited via sputtering including metals and semiconductors. One primary advantage to sputtering is its ability to cover large surfaces. On the other hand, sputtered films often suffer from a lack of uniform film thicknesses.

The films developed for this research utilized radio-frequency (RF) magnetron sputtering on a system located in Gilbert Hall. At the time this research was conducted, the system consisted of a single water cooled magnetron gun powered by a variable voltage power supply. It has since been upgraded to include a second gun and power supply. In addition to variable power capabilities, the system can be configured to heat and/or rotate the substrate. Target to substrate distance can also be varied manually. All of these variables affect film quality.

System base pressures on the order of 10^{-6} torr and sputtering gas pressures between 10 torr and 100 torr are typical. At the time of this research, argon, oxygen and argon-oxygen mix gases were available. Complete system documentation is stored electronically and on site.

Table 1 shows the parameters for six sputtered films. Note that the target to substrate distance was 1.5 inches in all cases.

Table 1: Sputtering Results											
		SPUTTER PARAMETERS									
DOPANT	**Film #**	**Date**	**Substrate**	**Nominal Power** (W)	**Substrate Temp**	**Base Pressure** (μTorr)	**Dep. Pressure** (mTorr)	**Dep. Gas Type/Press** (mTorr)		**Dep. Time** (h:mm)	**Appearance**
Potassium	K1	08/30/04	Fused Quartz	60	Ambient	0.65	5	Ar	3	1:45	Very clear
								O_2	2		
	K2	09/14/04	Fused Quartz	90	Ambient	0.74	5	Ar	3	1:46	Very clear
								O_2	2		
	K3	09/16/04	Fused Quartz	90	Ambient	0.69	5	Ar	0	1:46	Very clear
								O_2	5		
Indium	In1	08/12/04	Fused Quartz	90	Ambient	0.77	20	Ar	20	1:44	Clear
								O_2	0		
	In2	08/18/04	Fused Quartz	120	Ambient	0.80	20	Ar	20	1:44	Clear
								O_2	0		
	In3	08/20/04	Fused Quartz	60	Ambient	0.71	20	Ar	18	1:45	Clear
								O_2	2		

Pulsed Laser Deposition Films

Pulsed laser deposition (PLD) uses short duration, high energy pulses which ablate the target typically resulting in highly stoichiometric films. However, the material plume has a small cross section compared with sputtering discharge so film sizes are smaller and can suffer from a non-uniform thickness across the film.

For this study, films were made using a Neocera Pioneer 120 PLD system employing a Lambda Physik 248 nm KrF excimer laser located in the Tate Lab on the OSU campus (Weniger Hall, OSU). This system has the ability to vary substrate distance, temperature, laser energy density, pulse frequency, base and gas deposition pressures as well as laser beam (offset) scanning. The latter can assist in overcoming the problem of non-uniform film thickness mentioned previously.

Table 2: PLD Results											
		PLD PARAMETERS									
DOPANT	**Film #**	**Date**	**Substrate**	**Laser Fluence** (J/cm^2)	**Laser Power**[1] (mJ)	**Substrate Temp** (°C)	**Base Pressure** (mTorr)	**Dep. Gas Type/Press** (mTorr)		**Pulses** (#)	**Appearance**
Lanthanum	BTO1 1%	09/09/05	a-S_iO_2	1.94	28	400		O_2	3.0	9,000	Clear, slight rainbow
	BTO2 10%	09/12/05	a-S_iO_2		30	500		O_2	5.0	9,000	Cloudy, dusty
Undoped	1	11/10/05	a-S_iO_2		32	600		O_2	25	14,000	Clear
	2	11/22/05	MgO (100)		32	600		O_2	25	14,000	Clear
	3	02/08/06	Si/Ta		30	550		O_2	10		Clear
	4	02/15/06	MgO (100)		29	570		O_2	0	10,000	Clear
	5	02/16/06	Si/Ta				0.8	O_2	5		Clear

The lanthanum doped films were deposited on amorphous silicon dioxide and were developed to be tested for their n-type semiconducting characteristics. While the first undoped film was also deposited on amorphous silicon, the second and fourth undoped films were deposited on single crystal magnesium oxide (MgO) in an attempt to improve film characteristics through lattice matching. Finally, the third and fifth undoped films were deposited on silicon layered with tantalum. Aluminum contacts were then added to the BTO and these films were tested films for their dielectric characteristics. The target to substrate distance was 1.5 inches in all cases.
The energy at the entrance port was measured using a hand-held meter. Ten percent of this value was subtracted due to the absorption of energy by the glass at the laser entry point.

Laser fluence (energy per unity area) is calculated as: $\text{Fluence} = \dfrac{\text{Energy striking target}}{\text{Area of pulse mark}}$

The area of the mark left by laser pulse was found by multiplying the average length and width of the mark.

$$\text{Fluence} = \frac{\text{Energy striking target}}{\text{Area of pulse mark}} = \frac{28mJ = 0.10 \cdot 28mJ}{2.6mm \cdot 0.50mm} = 1.94 J / cm^2$$

Dielectric Films

Two undoped BTO films were developed for dielectric testing. Both were deposited onto a tantalum-silicon substrate via PLD; one was 100 nm and the other 450 nm thick. Aluminum was then deposited onto the BTO through a mask in order to create a matrix of metallic contact points. A block diagram is shown in Figure 23.

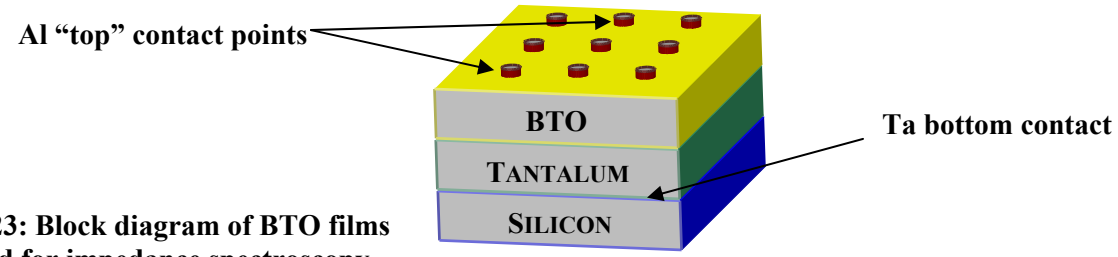

Figure 23: Block diagram of BTO films prepared for impedance spectroscopy

The tantalum served as the bottom contact while the aluminum dots served as an array of top contacts. Deposition of the aluminum contacts as well as the subsequent dielectric measurements were done by the Electrical Engineering Department at OSU.

EXPERIMENTAL RESULTS

X-ray Diffraction

X-ray diffraction (XRD) analysis was performed by the OSU chemistry department to determine the structural composition of the films. The analysis indicated single-phase BTO, but XRD is typically insensitive to impurities at a level lower than about 1%, and the dopants would be revealed only by small shifts in the lattice parameter, which were not measured. EPMA analysis conducted by the University of Oregon on one of the potassium-doped films revealed that no dopant was present in the film. It is likely that the potassium dopant evaporated out of the target and/or the film during the fabrication stage.

Figure 10 shows the X-ray diffraction pattern for undoped BTO from this study.

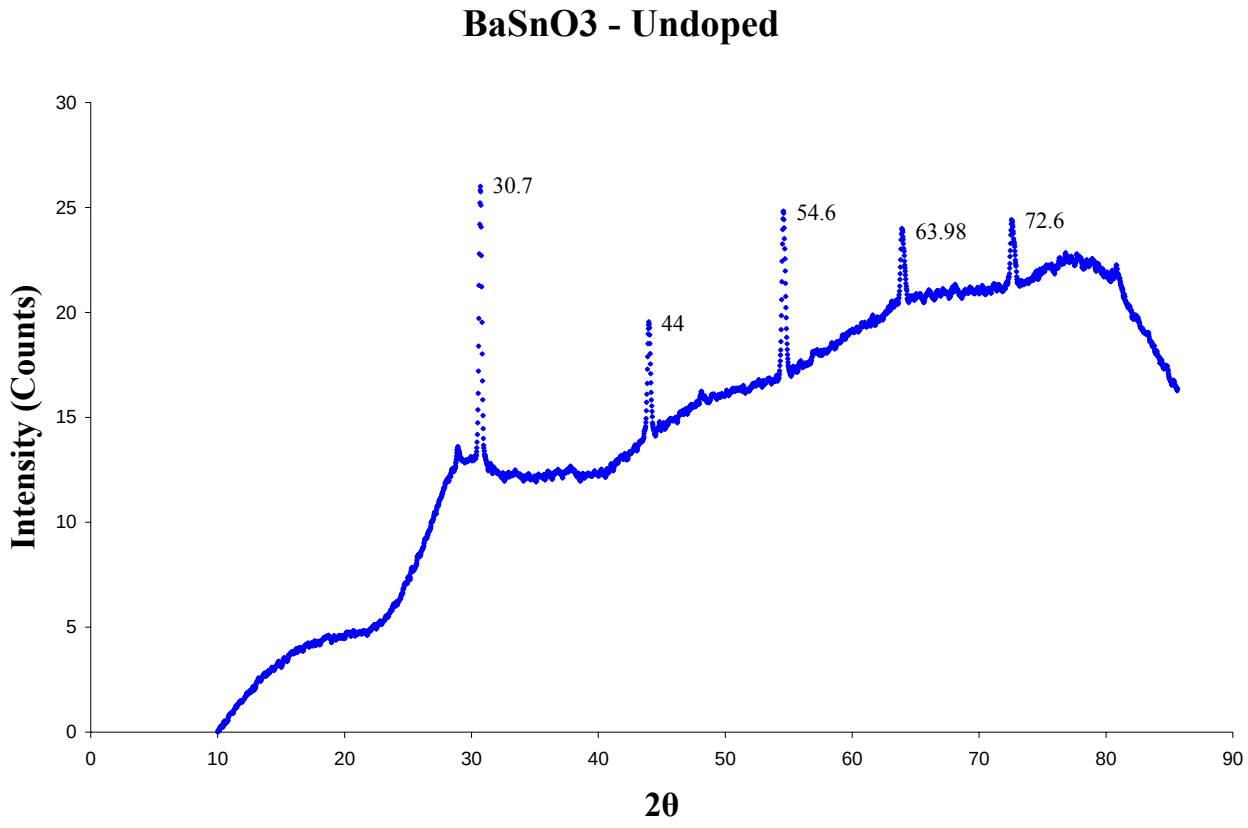

Figure 10: XRD pattern for undoped BTO

Shown below is the XRD pattern of undoped BTO (Figure 10, previous page) rescaled to facilitate comparison with the XRD pattern given by the Joint Committee on Powder Diffraction Standards (JCPDS) file 74-1300 given previously in this report. The peaks match reasonably well.

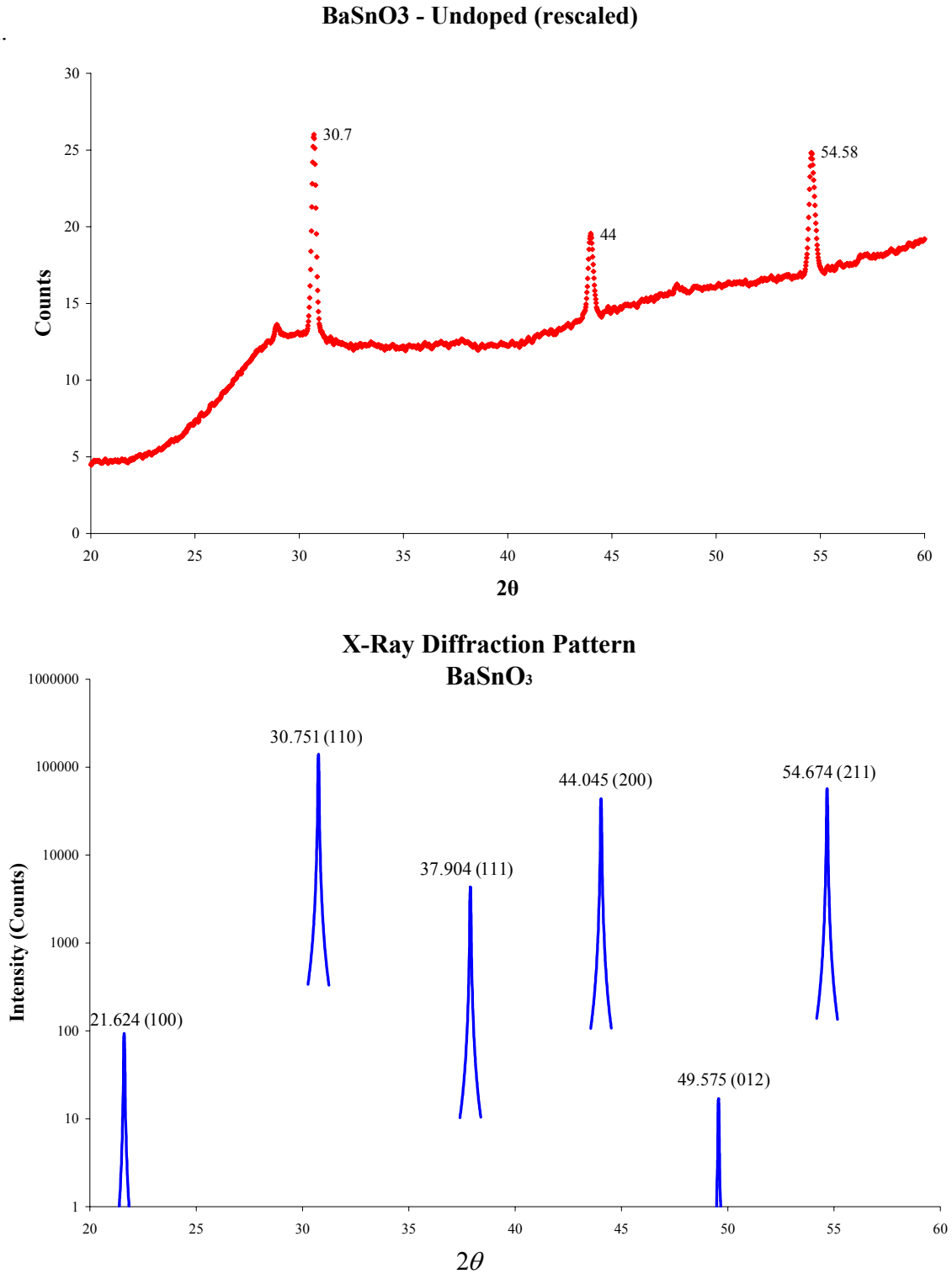

Figure 11: Comparison of undoped BTO XRD pattern (top) with standard file pattern.

The graph below (Figure 12) compares 10% lanthanum-doped BTO with the SnO_2 and $BaSnO_3$ powder diffraction files.

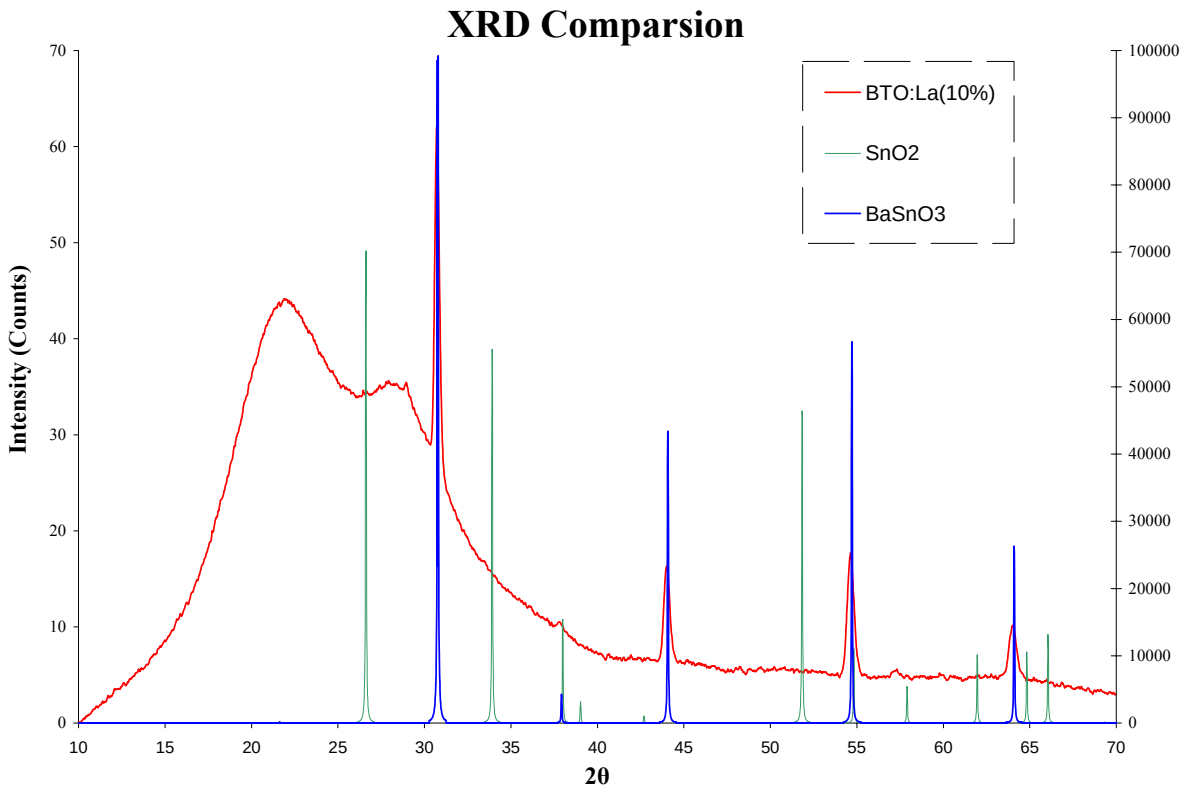

Figure 12: XRD comparison of $Ba_{0.9}La_{0.1}SnO_3$, $BaSnO_3$, and SnO_2

Optical Properties

The optical properties of the films are analyzed using an in-house spectrometer located in the McIntyre Lab (Weniger Hall, OSU). The fundamental goal is to determine the transparency of each film. To facilitate this, two scans are taken, one to measure the reflectance from and another the transmittance through the film. The film, optics and photodetector are contained in a "darkbox" with the monochromator and additional electronic equipment located adjacent to but outside of the darkbox. The film is clipped to a holder and the monochromator's beam projected through it and subsequently focused onto a detector. The film is rotated at an angle of about 10˚ with respect to the normal of the beam to facilitate the reflectance scan. For consistency, the film is left at the same angle for the transmittance scan. Once the laser has been focused onto the photodetector via two collimating lenses, the box is closed to block out any ambient light. Software sets into motion a process whereby monochromatic light of continuingly varying wavelengths is made to strike the film's surface. The amount of reflected and transmitted light is collected in nanometer-degree increments using in-house software. The data are then normalized to a third scan taken when no film (or substrate) is present in the sample holder. Raw data from the process is then imported to spreadsheet software, analyzed and then plotted. Additional software is used to determine film thickness, index of refraction and bandgap and will be discussed later in this paper.

All of the BTO films characterized for their optical properties, save one, remained highly transparent. The photograph below (Figure 13) shows the transparency of one of the BTO thin films.

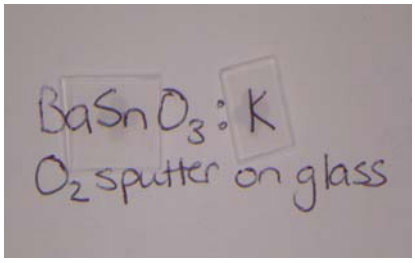

Figure 13: Potassium-doped BTO on glass

After the films are scanned by the spectrometer, data are imported to spreadsheet software, analyzed and then plotted. Three sets of data are available: 1) intensity transmittance data (t), intensity reflection data (r), and "raw" lamp data (l). From these three sets of data, a reflectance (R) spectrum, transmittance spectrum (T) and absorptance spectrum are generated as $R = \frac{I_r}{I_l}$ $T = \frac{I_t}{I_l}$ $A = \frac{T}{1-R}$ respectively. The purpose behind the first two calculations is to normalize the reflectance and transmittance data to the lamp, i.e., eliminate the source's (lamp) optical spectrum from the film's optical spectrum. The third calculation, based on the results of the first two, is a measure of the absorptance of the film. The absorption coefficient is of particular importance simply because it is a measure the transparency of the film. It bears repeating that the purpose of this branch of research is to develop thin films that are transparent in the visible spectrum, yet also have the ability to conduct and control the flow of electrical current. A further discussion follows below.

The chart below (Figure 14) was generated from data collected BTO film that was deposited on glass via RF sputtering. The target was doped with 10% potassium.

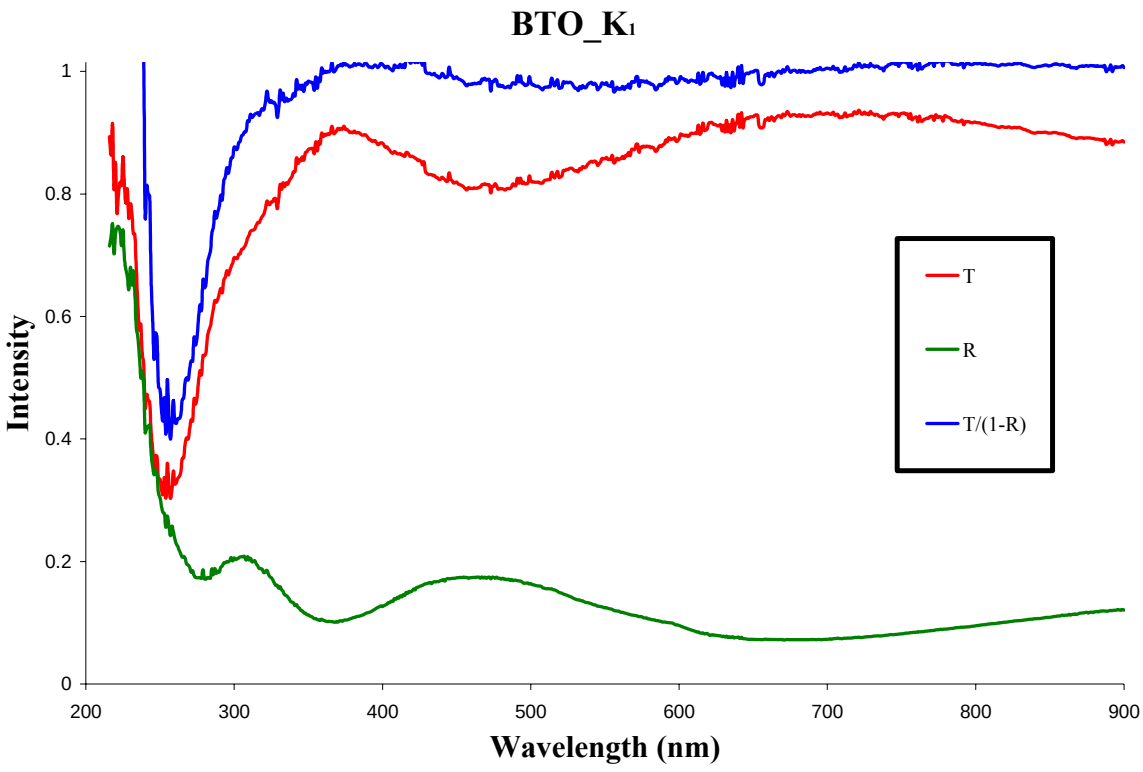

Figure 14: Optical transmittance T, reflectance R, and absorptance T/(1-R) of K-doped BTO

Notice that Figure 14 contains three plots. The green plot is an indication of the intensity of light reflected (reflectance, R) from the film as a function of wavelength. However, this plot is, in reality, the culmination of multiple reflections between the air-film and film-substrate interfaces as well as internal reflections within the film itself as shown in Figure 15 below.

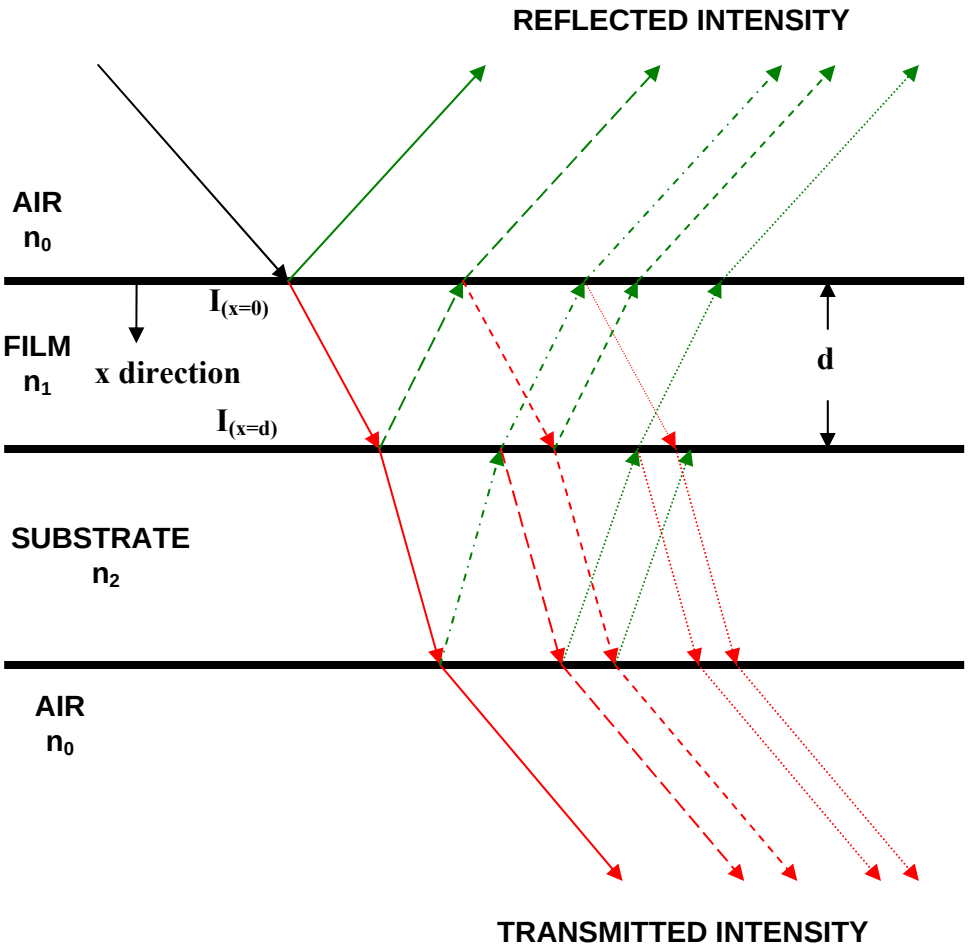

Figure 15: Optical transmittance and reflectance.

Likewise, the red plot is an indication of the light intensity transmitted (transmittance, T) through the thin film and is subject to the same qualification as the reflection plot. It should be noted that the reflections are evidenced by the intensity variations (undulations) in the plots.

The blue plot takes into account the air-film and film-substrate reflections and corrects for them by employing the *Lambert-Beer law*:

$$I(x) = I_0 e^{(-\alpha x)} \tag{1}$$

where I is the intensity of the light as a function of position, x within the film, I_0 is the intensity at x_0 and α is the absorption coefficient, a measurement of the rate at which the film absorbs (light) energy as the light traverses the film.

Now, if we assume that light incident on a film can be: a) reflected, b) transmitted or c) absorbed, then conservation of energy dictates that

$$R + T + A = 1$$

Now, at the instant light enters the film, its intensity has been reduced due to the reflection off of the front surface of the film. In this case the intensity is given by

$$I_{(x=o)} = 1 - R$$

Once the light has traversed the film's thickness, its intensity is given by

$$I_{(x=d)} = T$$

Forming a ratio of these two expressions yields an expression for the absorption coefficient as a function of the transmittance and reflectance.

$$\frac{I}{I_0} = \frac{T}{1-R} = \frac{e^{(-\alpha d)}}{e^{(-\alpha \cdot 0)}} = e^{(-\alpha d)}$$

Or solving for α gives

$$\alpha = -\frac{\ln\left(\frac{T}{1-R}\right)}{d} \tag{2}$$

It is important to note, however, that the Lambert-Beer law does not take into account the multiple reflections within the thin film itself [17] as illustrated in Figure 15. Also, there are assumptions that the reflection coefficients of the interfaces are low, the angle of incidence is small and the absorption by the film occurs in one pass through the film [18].

It is evident that the film above is highly transparent and non-absorbing. Other BTO films yielded similar characteristics.

The charts below (Figure 16) are the results of two more optical scans. The first is undoped BTO on glass (SiO_2) and the second is undoped BTO on MgO. The purpose for depositing on MgO was to "lattice match" the material to the substrate in order to improve the likelihood of witnessing photoluminescence. Although photoluminescence was not detected, it is notable that the film on the MgO substrate has less structure than the one on glass and it is very transparent.

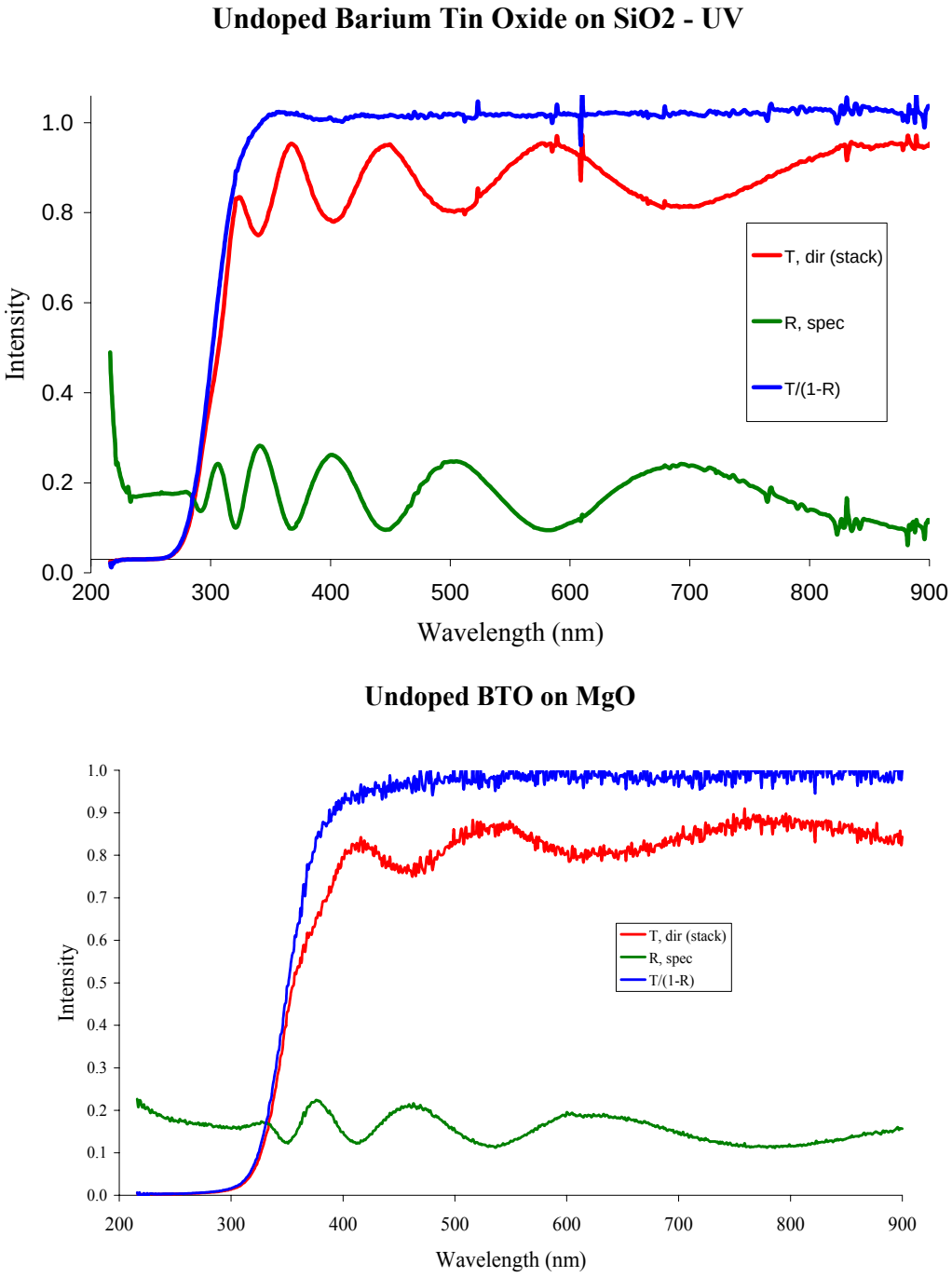

Figure 16: Comparison of optical scans for undoped BTO on SiO_2 (top) and MgO (bottom).

Additional software was used to extract relevant information about the thin films including the index of refraction, film thickness and optical bandgap. The following pages present a discussion based on the analysis of the data for undoped BTO on glass.

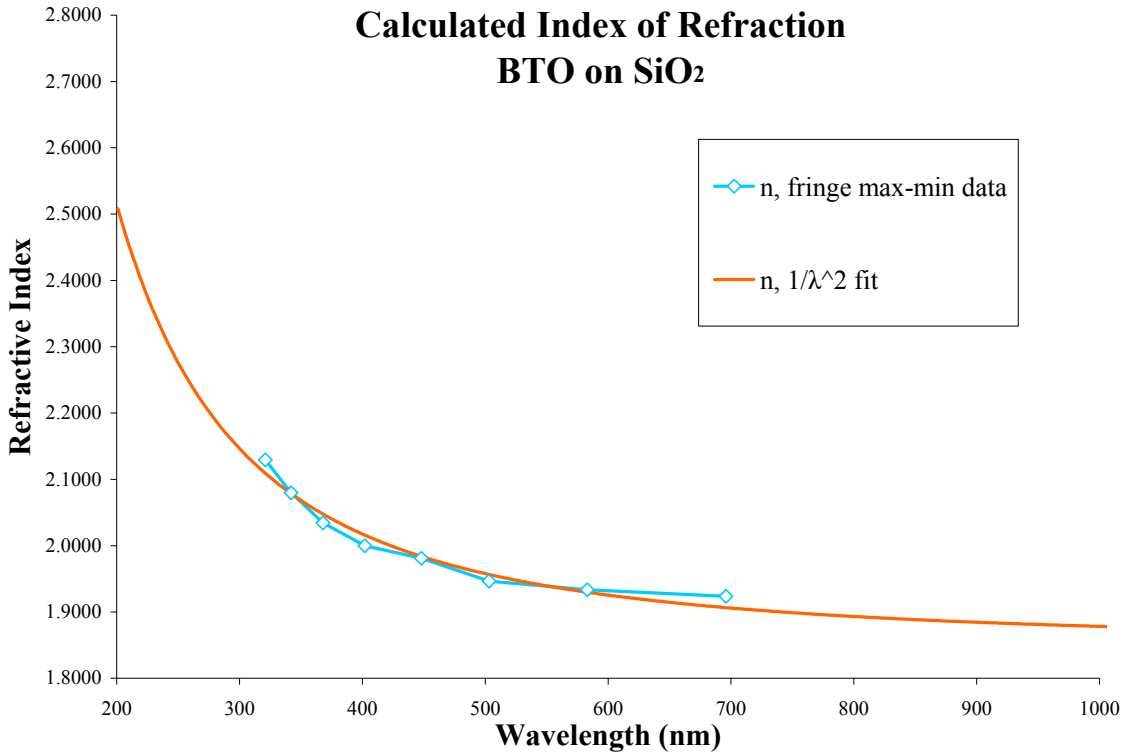

Figure 17: Extraction of the index of refraction of BTO on glass.

The index of refraction is the ratio of the speed of light in a given material to the speed of light in a vacuum ($n = c/v$) and indicates how the material will "govern" the light passing through it. It is well known that the index of refraction, *n*, is a function of wavelength[2] λ. Since wavelength and energy are functions of the properties of a given material, the index of refraction becomes an important indicator of material quality and usefulness.

An approximation of the relationship between the index of refraction and wavelength for normally dispersive media is given by the Cauchy relation as

$$n(\lambda) = A + \frac{B}{\lambda^2} + \frac{C}{\lambda^4} + \ldots \qquad (3)$$

where *A*, *B*, *C*, etc. are constants based on characteristics of the particular media including its resonance frequency [19]. It should be noted that dispersion, the way in which the index of

refraction changes with respect to a change in wavelength $(dn/d\lambda)$, is negative for transparent materials.

It is equally well known that the relationship between wavelength λ, index of refraction *n* fringe number *m* and film thickness *d* is given by

$$\lambda = \frac{2nd}{m} \Leftrightarrow n = \frac{m\lambda}{2d} \tag{4}$$

The results from the spectrometry yields information about the fringe numbers as evidenced by Figure 16. Then, using (4), singular *n*-values can be determined. Using these values of *n* and linear regression applied to (3) yield the smooth curve in Figure 17.

Had the film thickness *d* been know beforehand, the Sellmeier equation [20] given by

$$n^2(\lambda) = 1 + \frac{B_1\lambda^2}{\lambda^2 - C_1} + \frac{B_2\lambda^2}{\lambda^2 - C_2} + \frac{B_3\lambda^2}{\lambda^2 - C_3} + \ldots \tag{5}$$

can be used to more precisely determine the index of refraction. For this study, the film thickness was not measured by any physical means, so the Sellmeier equation was not used for the purpose of finding the index of refraction.

Once the film thickness was determined by using (3) and (4) above, the reflectance and transmittance spectra of the films were developed theoretically and compared to the experimental spectra as shown in Figures 18 and 19 below. The variance between theoretical and experimental is minimal.

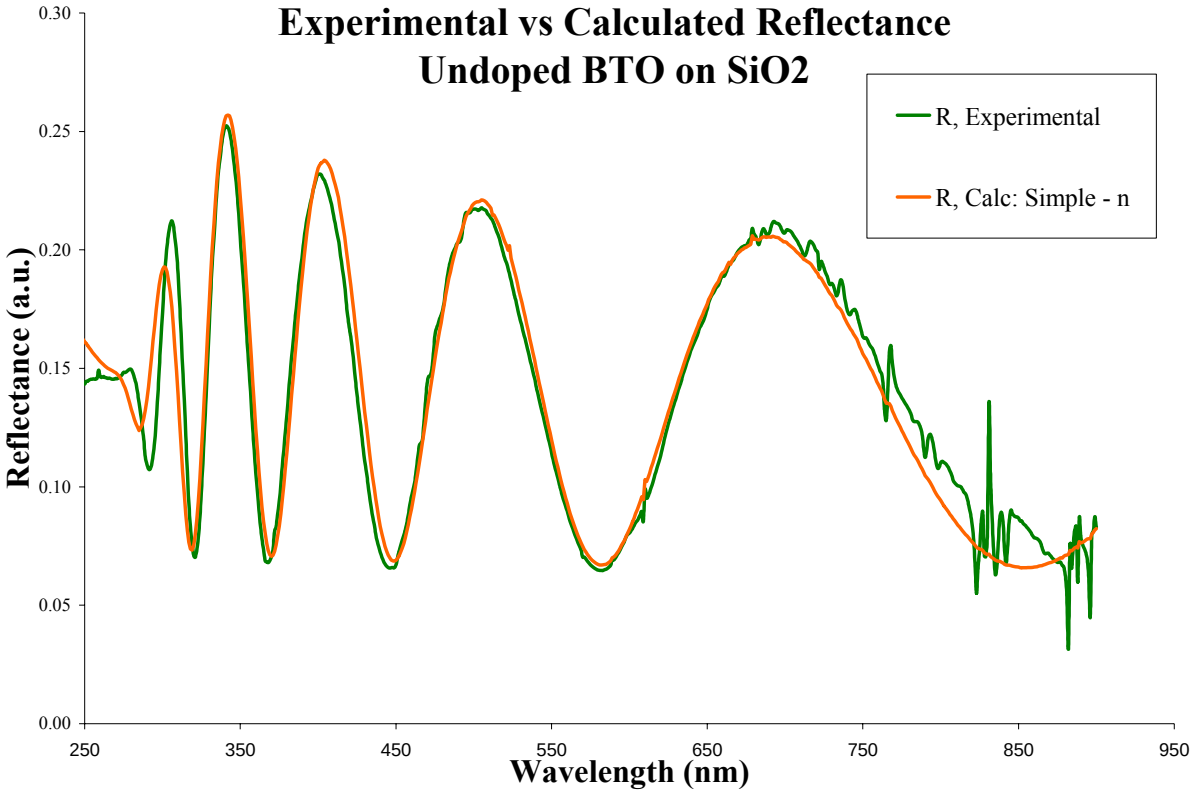

Figure 18: Comparison of experimentally and calculated reflectance.

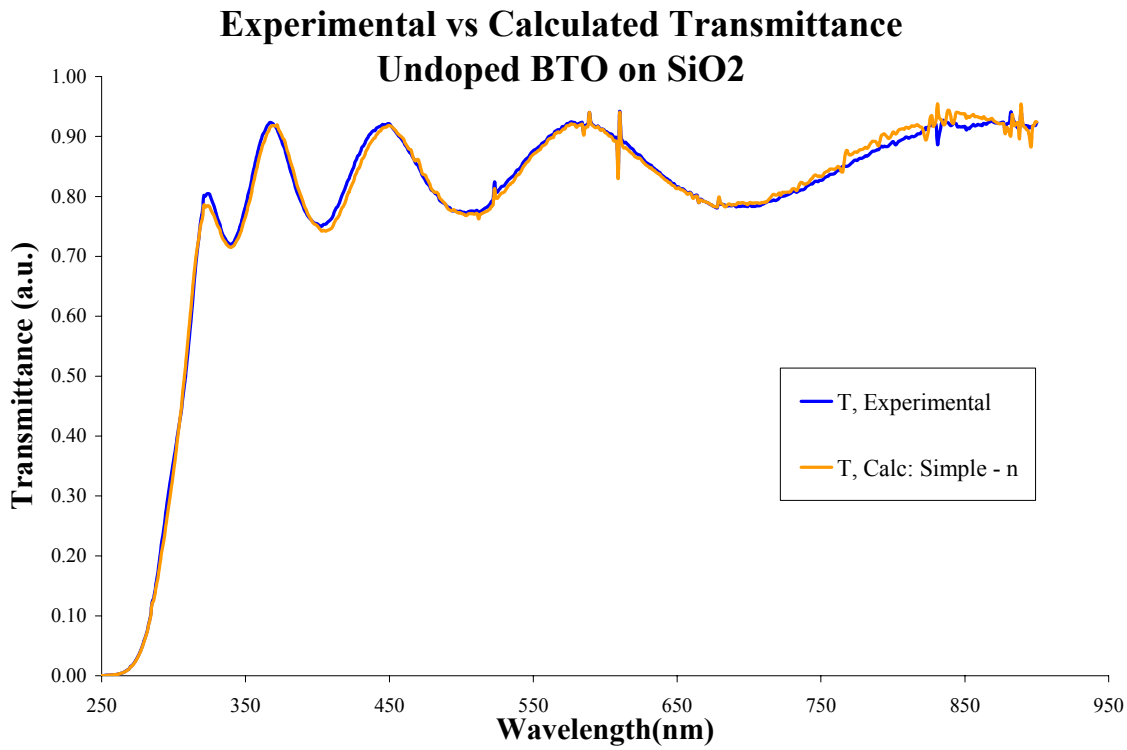

Figure 19: Comparison of experimentally and calculated transmittance.

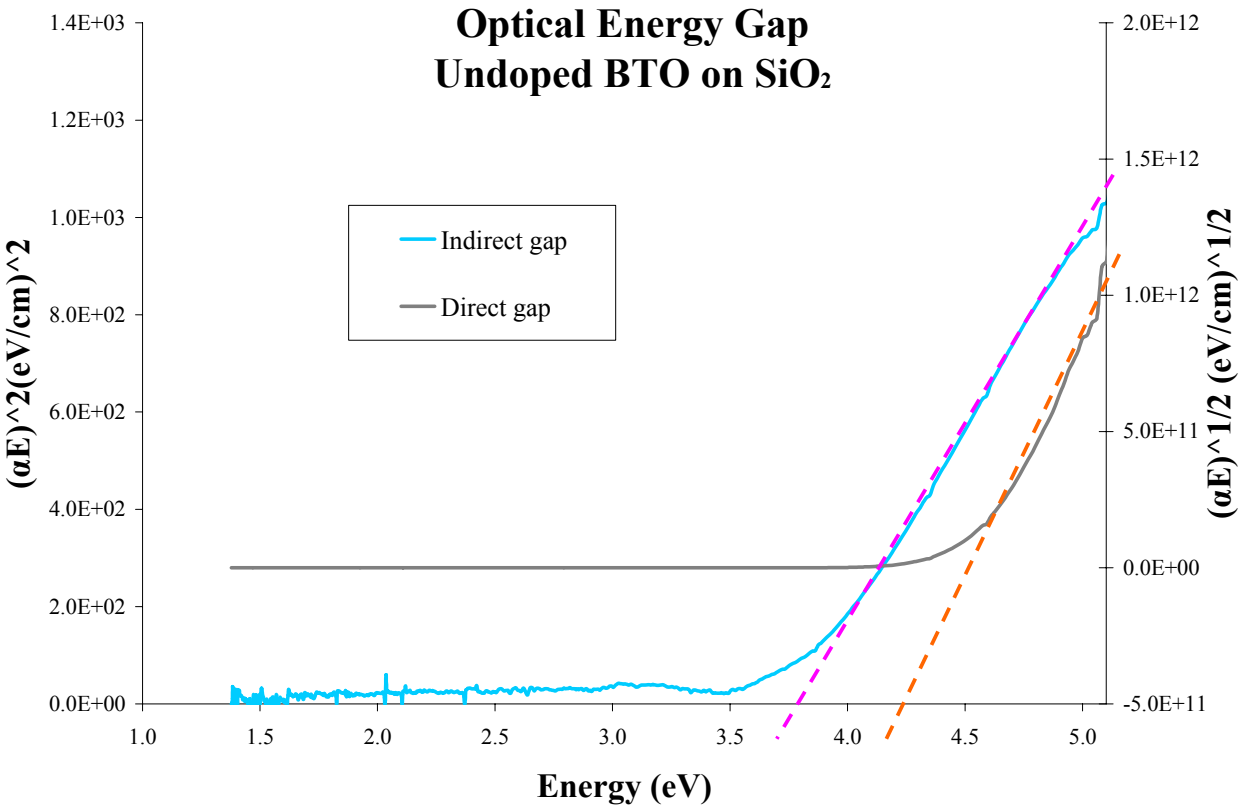

Figure 20: Extrapolation of band gap energy value

It is an accepted practice to plot both $(\alpha E)^2$ and $(\alpha E)^{\frac{1}{2}}$ a function of E (Figure 20) because, in principle, it may not be known whether the material has a direct or indirect optical bandgap. The plot of $(\alpha E)^2$ is for direct bandgap materials while the plot of $(\alpha E)^{\frac{1}{2}}$ is for indirect bandgap materials. Graphing these relationships side-by-side may reveal that information by virtue of the plot that exhibits a more rapid onset. If that determination can be clearly made, the "linear" portion of the graph is extrapolated to intersect with the energy axis (broken lines, Figure 20) to determine the bandgap.

It is not apparent in these graphs for BTO which one is a better fit, however previous results have determined that BTO is an indirect bandgap material. Furthermore, the graph confirms the previously accepted value of 3.7 eV.

It is important to note that for materials with well documented bandgap values, procedural calculations vary from that above. For example, it has been determined that plotting $(\alpha E)^{\frac{1}{3}}$ *vs.* E yields the most accurate bandgap values for amorphous silicon [18].

The optical bandgap can also be "extracted" by plotting the absorption coefficient against energy as shown in Figure 21a. Typically, the sharp rise in the linear graph is indicative of the onset of absorption and thereby revealing the bandgap. However, a first look at Figure 21a might lead one to believe that the bandgap may be on the order or 4.2 eV.

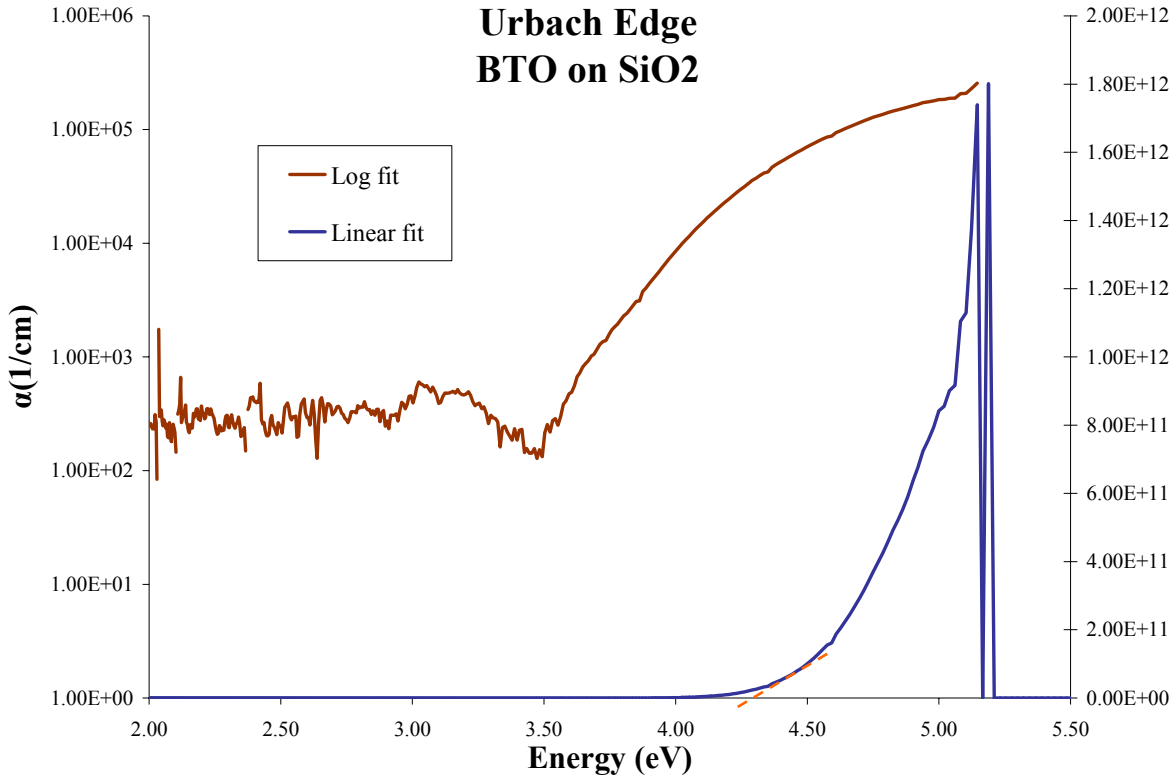

Figure 21a: Optical Edge

The linear plot can be enhanced by rescaling the left ordinate axis to include small negative numbers (10^{0} → 10^{-11}) and rescaling the right ordinate axis to include smaller positive numbers (10^{12} → 10^{7}). The result of this rescaling (zoom effect), shown in Figure 21b reveals the bandgap energy of approximately 3.70 eV.

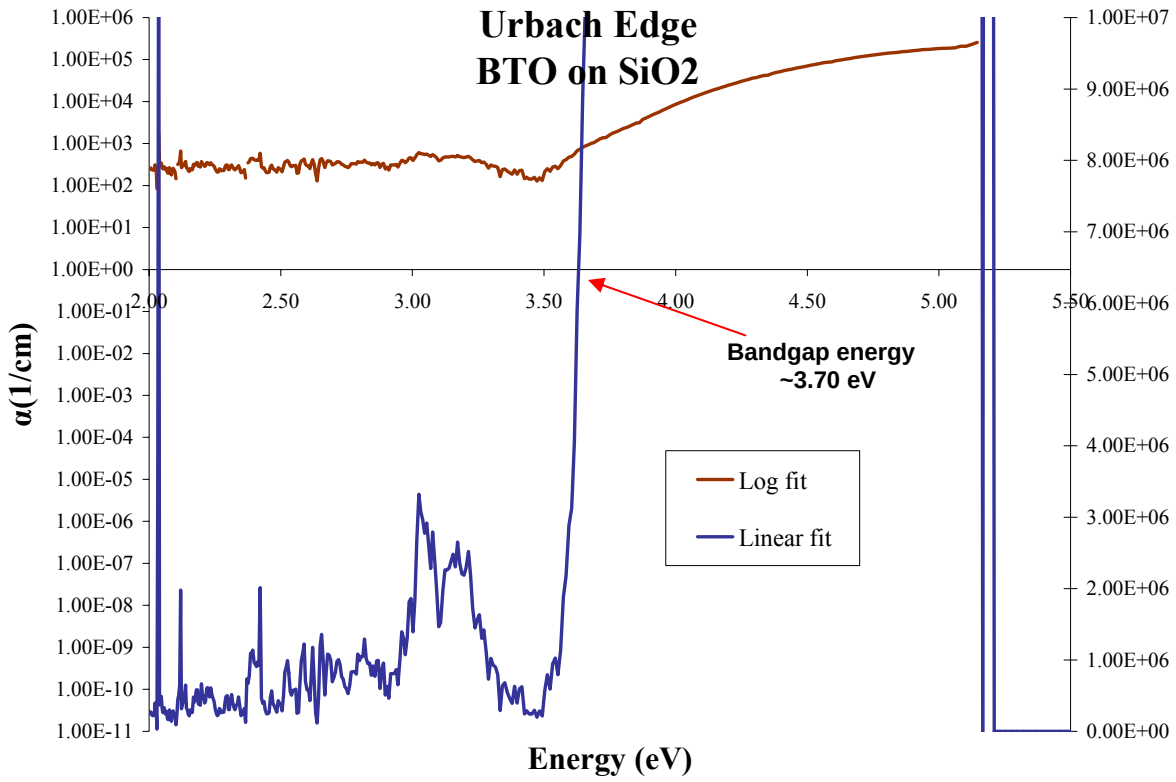

Figure 21b: Urbach Edge - rescaled

Photoluminescence

The undoped films were analyzed by the OSU chemistry department for indications of photoluminescence. The spectrum for the first film is shown in Figure 22. The solid line is photoluminescence from the target, the peak of which appears at first not to correlate to the 905 nm NIR peak found by Mizoguchi et al [10]. However, the range of the detector truncates the signal at longer wavelengths so, in fact, the correlation does exist. The dashed line has been added to illustrate this.

The signal from the films is very weak, and consists of two narrow, small peaks roughly in the position of the IR PL of the powder (Figure 22). Initially, it was thought that the two peaks, appearing at the same positions for two different excitation frequencies may well be from the thin film and correspond to the IR emission found in $BaSnO_3$ powder. However, no sensible mechanism for the peak shape could be found, so the origin remains unclear. One theory was that thin-film interference might be suppressing the peak center. To test for this possibility, the experiment could be redone using two films of different thicknesses. This would shift the relative peaks between the two films.

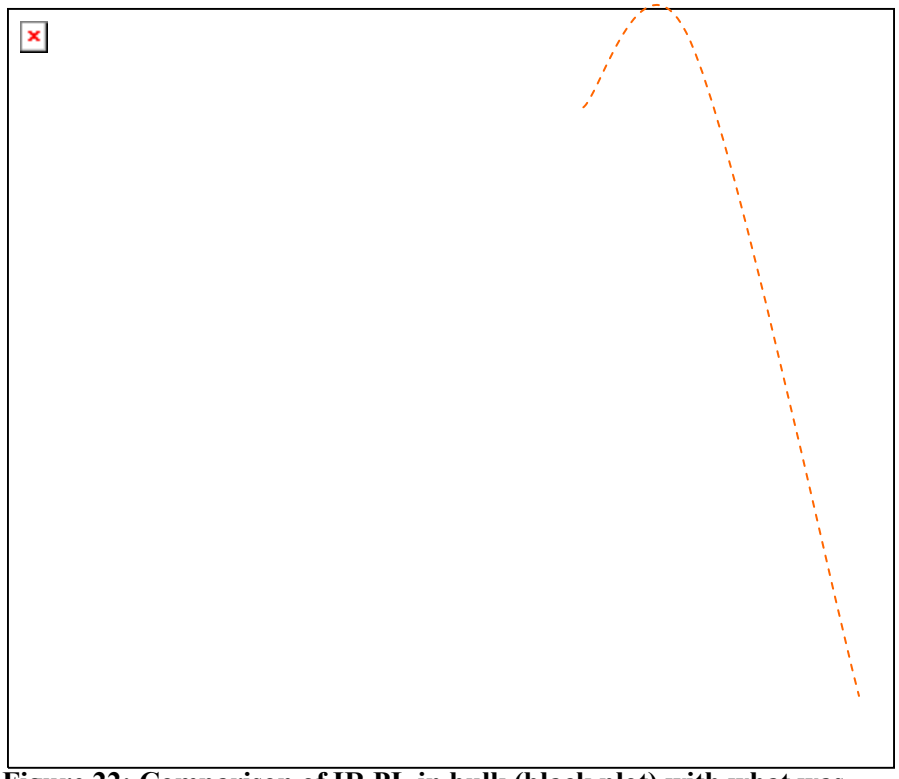

Figure 22: Comparison of IR PL in bulk (black plot) with what was initially thought to be IR PL in the thin films (red, green plots).

In any event, the mechanism for photoluminescence in the powder is still under debate and could be due to a secondary phase in the material.

Electrical Properties

Resistance Measurements

The films were initially tested for conductivity using a two-probe method consisting of touching the leads of a digital multimeter (DMM) set to resistance onto various points of the film's surface. In each case, the films measured infinite resistance indicating no semiconducting characteristics. If any resistance value is measured, the film would have been processed further using the Hall Measurement System located in the Tate Lab (Weniger Hall, OSU) however, because they were so highly insulating, Hall measurements were not made on the films.

Dielectric Characteristics

The films were analyzed for their low-frequency (100 Hz – 1 MHz) dielectric characteristics using Hewlett-Packard LCR electronic measuring equipment and in-house analysis software. The equipment measures capacitance and conductance and the software calculates the real and imaginary parts of the permeability of the film as well as the film's loss tangent. If the results are favorable, the films are further analyzed for there dielectric breakdown characteristics.

Neither film showed promise of being a good candidate as a dielectric material. The 100 nm film yielded dielectric constant of 0.01 and the 450 nm film yielded dielectric constants between 50 and 100+. Several possibilities were proposed: 1) A thickness gradient developed when the film was deposited over the 25 mm^2 area, causing erroneous readings; 2) there was a problem with the films' density; or 3) titanium oxide may have developed due the high deposition temperature (~450 °C).

In order to mitigate the creation of tantalum oxide, gold was deposited over the tantalum using evaporation techniques. The research ended before the fabrication of the thin films was completed, so they were not sent for dielectric testing.

Breakdown measurements were not able to be made on either film because of their poor dielectric characteristics. The expected range of values is 1-20.

Table 3: Permittivity & Loss Tangent Results			
Sample ID:	F24Oct05	BTO4.5K	BTO1K
Sample Material:	*HafSOx/Phos	BTO	BTO
Thickness (Angs.):	2300	4500	1000
Deposition Method:	spin coat	PLD	PLD
Top Contact:	Al	Al	Al
Bottom Contact:	Ta	Ta	Ta
Substrate:	Si	Si	Si
Device Area (cm^2):	0.011	0.011	0.011
Dot Position:	5,3	7,7	3,4
Relative Permittivity at 1 kHz:	8.69	4.07	0.01
Loss Tangent at 1 kHz (%):	2.16	94.19	254647908.95
*Sample result for comparison purposes			

Shown on the following pages, for comparison purposes, are the dielectric characteristics of (Ph)-doped "HafSOx," which is a considered a good dielectric material and the 450 nm BTO film.

Ideally, capacitance should stay constant with respect to frequency. The HafSOx film does just that while the BTO film varies dramatically.

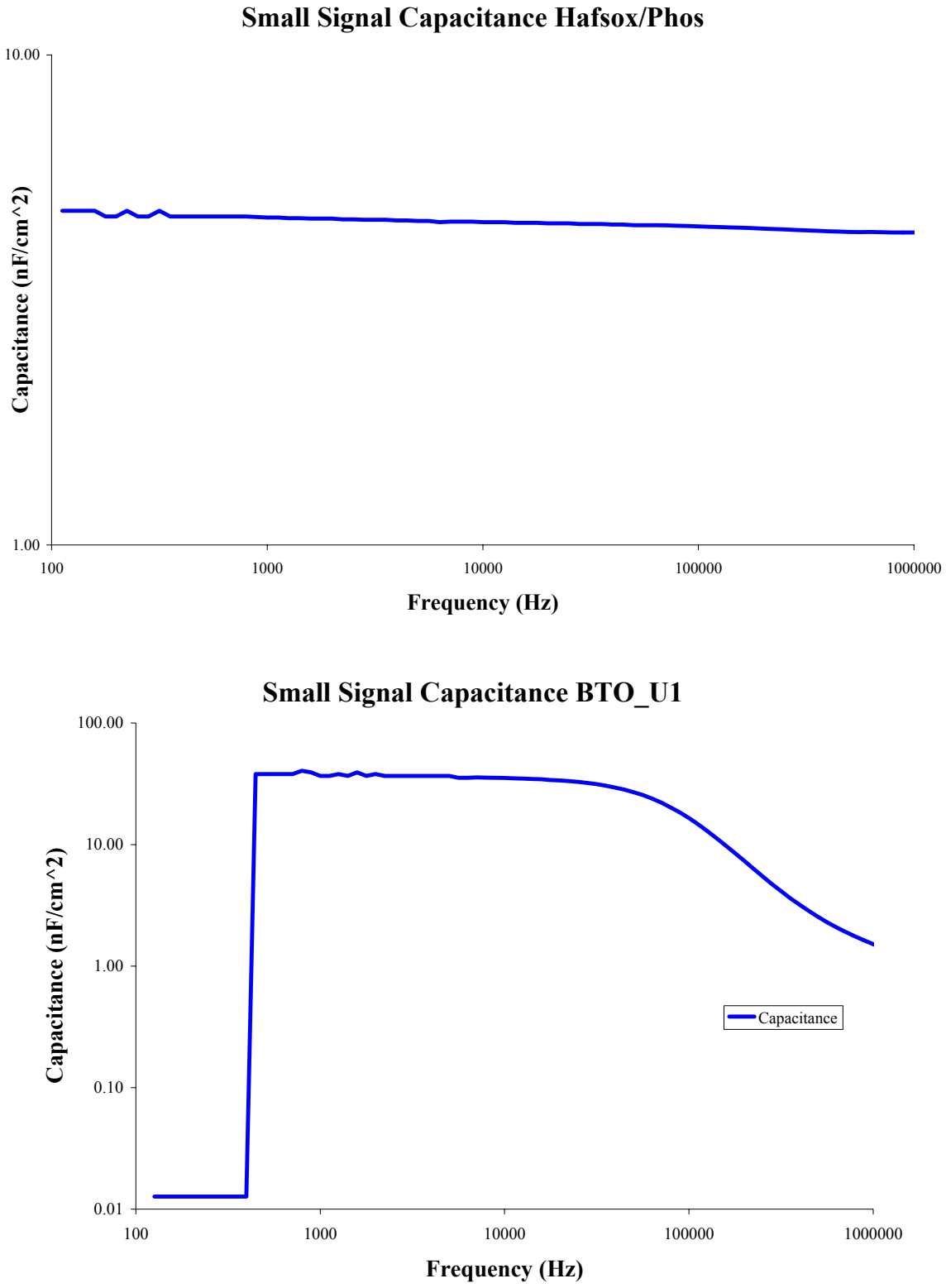

Figure 24: Comparison of small signal capacitance between HafSOx (top) and BTO (bottom).

Ideally, a capacitor should exhibit no conductance (infinite resistance) when faced with a DC source (0 Hz). Then, as frequency increases, conductance should increase exponentially. The BTO film exhibits high conductance at low frequency.

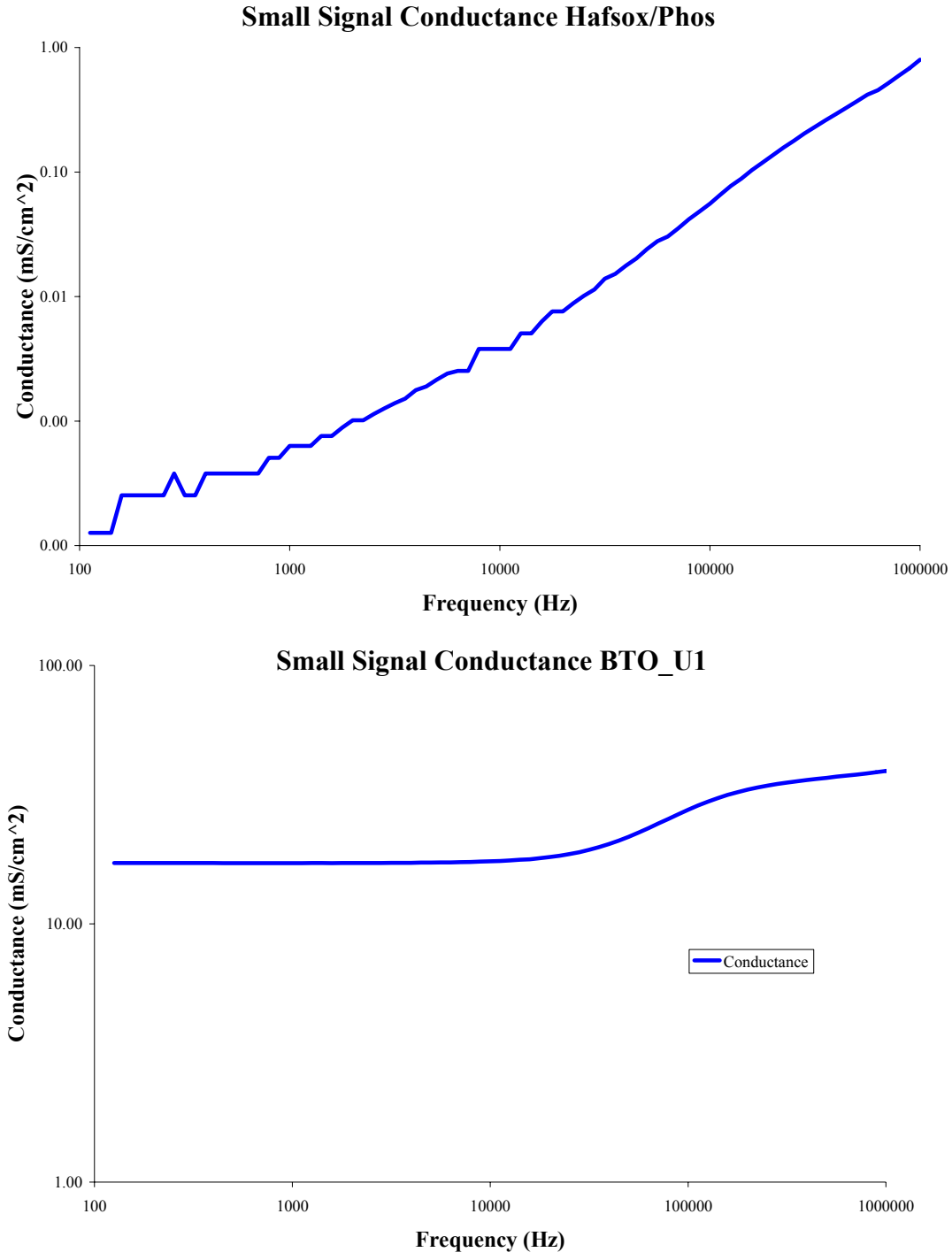

Figure 25: Comparison of small signal conductance between HafSOx (top) and BTO (bottom).

The permittivity of a capacitor should stay relatively constant with frequency. The HafSOx film does just that while the BTO film does not.

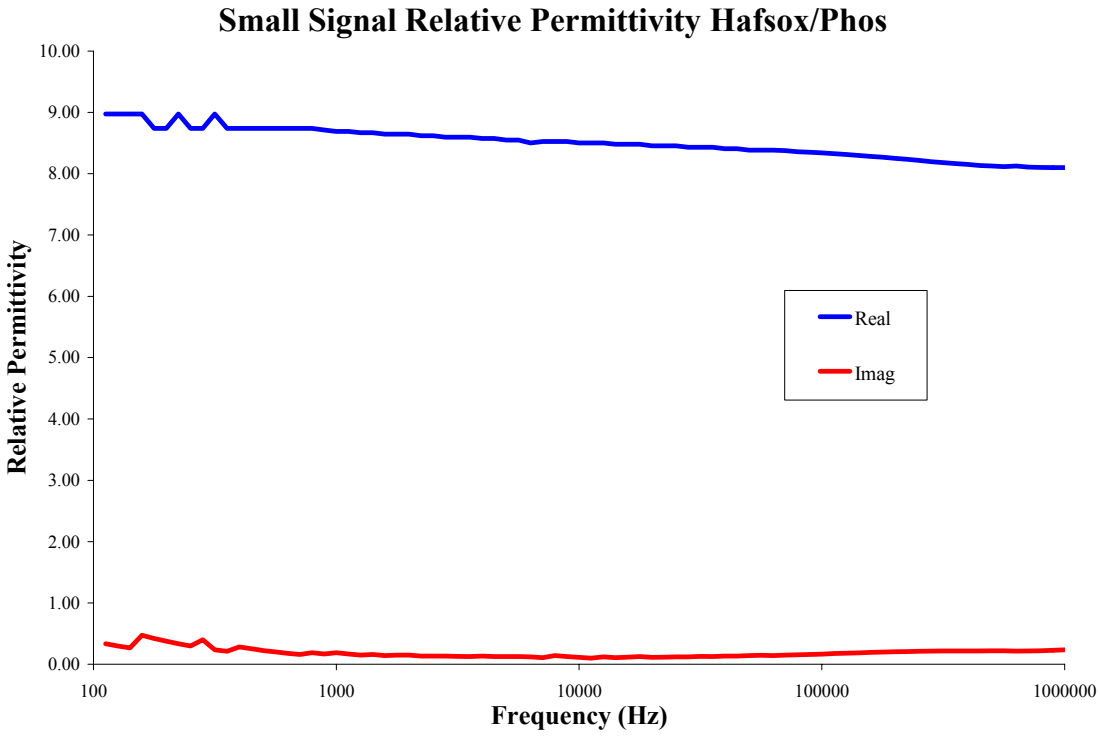

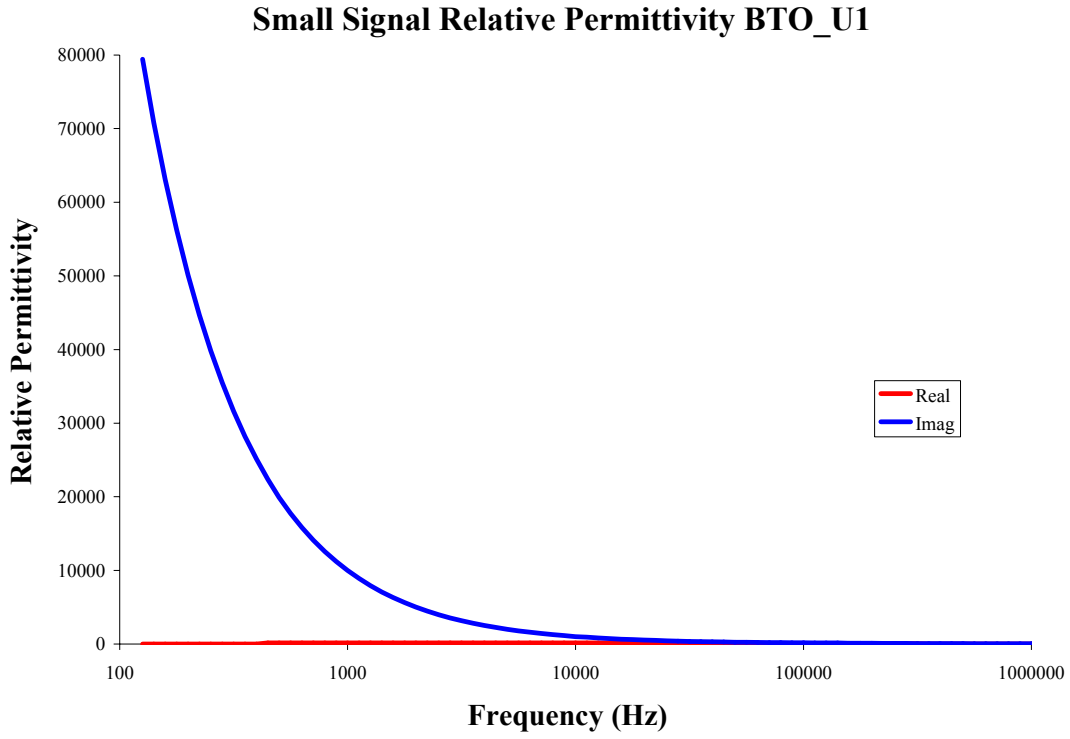

Figure 26: Comparison of small signal capacitance between HafSOx (top) and BTO (bottom).

The loss tangent is a measure of the "absorbency" a capacitor's dielectric. Ideally the loss tangent remains constant with respect to frequency, but will eventually deteriorate as frequency continues to increase. Though it appears that the loss tangent varies noticeably with the HafSOx film, notice that the range of the vertical scale is small. The BTO film bears no resemblance to a normally functioning capacitor.

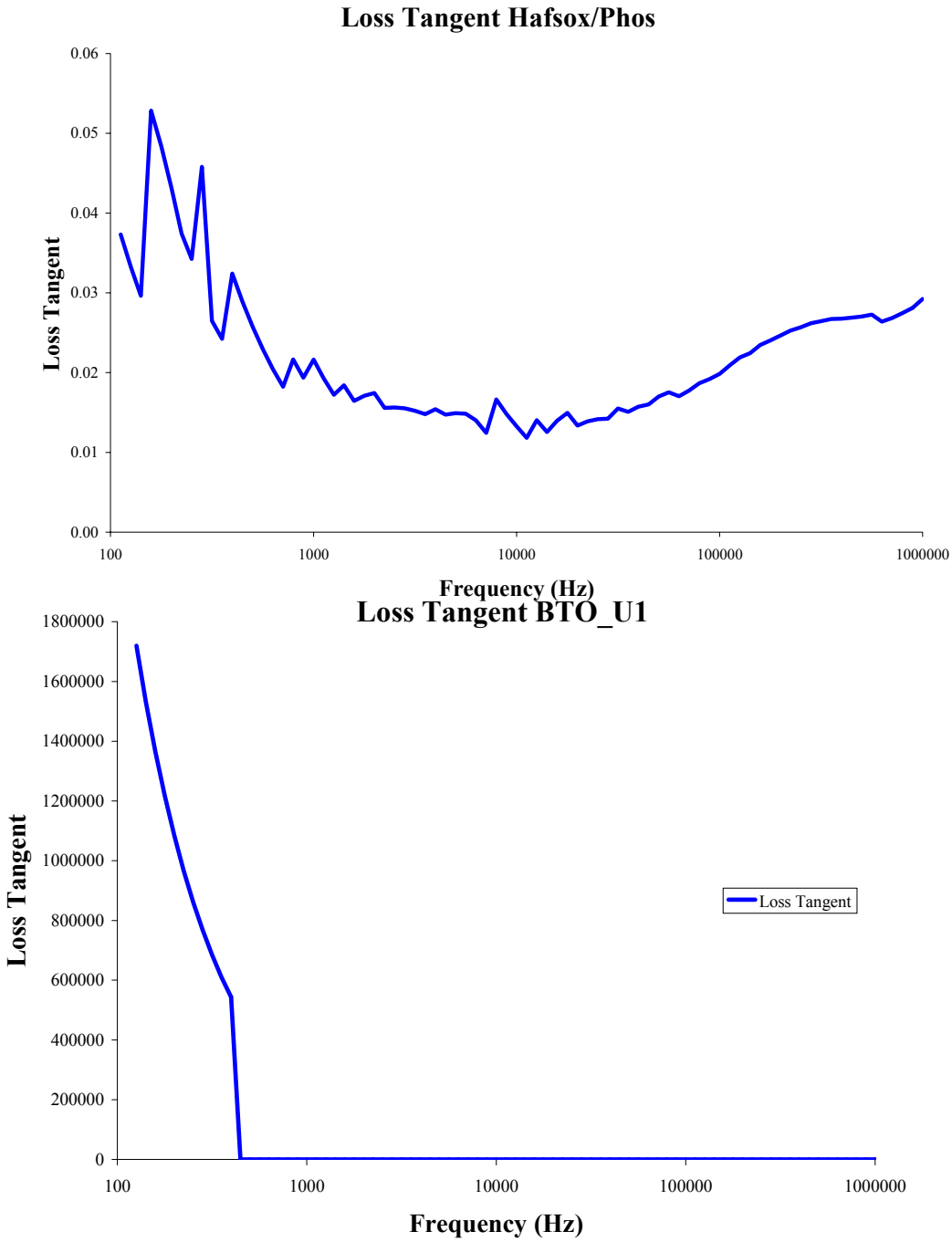

Figure 27: Comparison of loss tangent between HafSOx (top) and BTO (bottom).

CONCLUSIONS AND SUGGESTIONS FOR FURTHER STUDY

High quality, oriented films were produced on various substrates with optical bandgaps ranging between 3.7 eV & 4.4 eV. The undoped films were both highly insulating and transparent making them potential candidates in gas-sensor applications and as insulating layers in transparent transistors. The BTO films exhibited very strong interference fringes in the visible and near IR, indicating that the film surface and film/substrate interfaces are very smooth. Films did not show evidence of photoluminescence that had been reported in the bulk. Films doped with potassium, indium and lanthanum remained highly transparent but failed to exhibit any semiconducting characteristics.

Semiconductor characteristics may be realized as they have been in bulk form if a) target density can be improved and, b) target dopant concentration can be maintained. Cobalt-doped BTO has shown p-type conductivity in powder form and may warrant investigation in thin-film form.

It may also prove worthwhile to investigate how much dopant can be put into each film. By carefully measuring and then monitoring the lattice parameters, the solubility of BTO can be determined. As the dopant is added, the lattice parameters will change until maximum soluability is reached at which time the lattice parameters will no longer be affected.

Finally, dielectric testing could be repeated and results possibly improved, by using substrates in which the tantalum has been overlaid with gold. This should mitigate the creation of tantalum oxide.

ACKNOWLEDGEMENTS

I owe huge debt of gratitude to Professor Janet Tate who stuck by me unwaveringly through a series of fits and starts in completing this work. Her patience is comparable only to that of Job's. Professor Tate is a truly rare individual; an amazing educator, thinker and mentor. Her open door/open mind policy is invaluable to her students and, I suspect, her colleagues. Never have I gone away from her office or her classroom without both an answer and a challenge to think. Also, many thanks to the members of Dr. Tate's research group, especially Paul Newhouse, Robert Kykyneshi, and James Osborne. Thanks also to Peter Hersh and Cheol-Hee Park (OSU Chemistry) for fabricating my BTO targets and analyzing my films for photoluminescence. Finally, thanks to the members of Dr. Wager's engineering research group for providing me with substrates and especially to Celia Hung for analyzing my films for their dielectric characteristics.

REFERENCES

[1] Lampe, U., Gerblinger, J., and Meixner H., "Carbon monoxide sensors based on thin films of $BaSnO_3$," *Sensors and Actuators B,* vol. 25, pp. 657-660, Apr. 1995.

[2] Lampe, U., Gerblinger, J., Meixner H., "Nitrogen oxide sensors based on thin films of BaSnO3," *Sensors and Actuators B*, vol. 26, pp. 97-98, 1995

[3] Ostrick B., Fleisher M., Lampe U., and Meixner H., "Preparation of stoichiometric barium stannate thin films: Hall Measurements and gas sensitivities." *Sensors and Actuators B*, vol. 44, pp. 601-606, Apr. 1997.

[4] Upadhyay, S. and Parkash, O., "Preparation and characterization of barium stannate $BaSnO_3$," *Journal of Materials Science Letters*, vol. 16, pp 1330-1332, April 1997.

[5] Fleisher M. and Meixner H., High-Temperature Hall Measurements on $BaSnO_3$ Ceramics," *J. Am. Ceram. Soc.*, 80 [8] pp. 2153-56, 1997.

[6] Upadhyay, S, Parkash, Om., and Kumar, D., "Synthesis, structure and electrical behavior of lanthanum-doped barium stannate." *Journal of Physics D: Applied Physics*, vol. 37, pp. 1483-1491, 2004.

[7] Parkash, O., Kumar, D., Stivastav, K., and Dwived, R. "Electrical conduction behavior of cobalt substituted $BaSnO_3$," *Journal of Materials Science*, vol. 36, pp. 5805-5810, Aug. 2001.

[8] Cerda, J., Arbiol, J., Dezanneau, G., Diaz, R., & Morante, J., "Perovskite-type $BaSnO_3$ powders for high temperature gas sensor applications," *Sensors and Actuators B*, vol. 84, pp. 21-25, 2002.

[9] Reddy, C., Manorama, S. Rao, V. "Preparation and characterization of barium stannate: application as a liquefied petroleum gas sensor," *Journal of Materials Science: Materials in Electronics*, vol. 12, pp. 137-142., 2001

[10] Mizoguchi, H, Woodward, P. Park, C., and Keszler, D. "Strong Near-Infrared Luminescence in $BaSnO_3$," *Journal of the American Chemical Society*, vol. 126, pp. 9796-9800. Jul. 2004

[11] Unknown. (2010, November 28). Wikepedia. Perovskite (Structure). Retrieved from http://en.wikipedia.org/wiki/Perovskite_(structure).

[12] Megaw, H. "Crystal structure of double oxides of the perovskite type." *Proceedings of the Physical Society*, vol. 58, part 2, pp. 133-152, Mar. 1946.

[13] Mizoguchi, H. Eng, H, & Woodward, P. "Probing the Electronic Structures of Ternary Perovskite and Pyrochlore Oxides Containing Sn^{4+} or Sb^{5+}," *Inorganic Chemistry*, vol. 43, pp. 1667-1680, 2004.

[14] Shannon, R.D. and Prewitt, C.T. "Effective Ionic Radii on Oxides and Flourides." *Acta Cryst* B25, 925, May 1968

[15] Zhang, W., Tang, J., & Ye, J. "Photoluminescence and photocatalytic properties of $SrSnO_3$ perovskite," *Chemical Physics Letters*, vol. 418, pp 174-178, Oct 2005.

[16] Pontes, F., Pintheiro, Cl., Longo, E., Leite, E., de Lazaro, S., Magnani, R., Pizani, P., Boschi, T., & Lanciotti, F., "Theoretical and experimental study on the photoluminescence in $BaTiO_3$ amorphous thin films prepared by the chemical route," *Journal of Luminescence*, vol. 104, pp. 175-185, Jan. 2003.

[17] Jacob, W., von Keudell, A., and Schwarz-Selinger, T., "Infrared Analysis of Thin Films: Amorphous, Hydrogenated Carbon on Silicon," *Brazilian Journal of Physics*, Vol. 30, No. 3, Sept. 2000

[18] Hishikawa, Y., Nakamura, N., Tsuda, S., Nakano, S., Kishi, Y., Kuwano, Y., *Japanese Journal of Applied Physics*., Vol. 30, No. 5, pp. 1008-1014, May 1991
[19] Pedrotti, F., Pedrotti, L.S., and Pedrotti, L.M. "Introduction to Optics" 3rd ed. Pearson Education, 2007.
[20] Yang, K., French, R., and Tokarsky, E., "Optical properties of Teflon® AF amorphous fluoropolymers," *J. Micro/Nanolith,* 7(3), Jul-Sep 2008)